Forecasting constraints on nonthermal light massive relics from future CMB experiments (CMB-S4/Simons Observatory)

Arka Banerjee,[1] Abhik Bhattacharjee,[2,*] Subinoy Das,[3] Anshuman Maharana,[2] and Ravi Kumar Sharma[4,†]

[1]Department of Physics, Indian Institute of Science Education and Research, Homi Bhabha Road, Pashan, Pune 411008, India

[2]Harish-Chandra Research Institute, A CI of Homi Bhabha National Institute, Chhatnag Road, Jhunsi, Prayagraj, Uttar Pradesh 211019, India

[3]Indian Institute of Astrophysics, Bengaluru, Karnataka 560034, India

[4]Institute for Theoretical Particle Physics and Cosmology (TTK), RWTH Aachen University, Sommerfeldstraße 16, D-52056 Aachen, Germany

(Received 16 June 2025; accepted 6 January 2026; published 6 February 2026)

Precise measurements of the cosmological impact of dark sector relics can shed light on physics beyond the Standard Model. In this work we present Fisher forecasts on *nonthermal light massive relics (LiMR)* models for a CMB Stage IV-like experiment and the Simons Observatory—particularly focusing on a model of inflaton/moduli decay giving rise to nonthermally distributed dark sector particles, and also comparing our results with those for sterile particles following the Dodelson-Widrow distribution. Two independent parameters, the effective number of extrarelativistic species $\Delta N_{\rm eff}$ and the effective mass $M_{\rm sp}^{\rm eff}$ of the relic, influence linear cosmological observables. We find $\Delta N_{\rm eff}$ to be more tightly constrained with $\sigma(\Delta N_{\rm eff}) \sim 10^{-3}$, for a less abundant, heavier LiMR, which becomes fully nonrelativistic around matter-radiation equality than a more abundant, lighter LiMR, which becomes fully nonrelativistic just after recombination, for which $\sigma(\Delta N_{\rm eff}) \sim 10^{-2}$. The uncertainties on $M_{\rm sp}^{\rm eff}$ differ by a factor of ∼3 between the two cases. Our analysis also reveals distinct parameter correlations: the phenomenological parameters $\{\Delta N_{\rm eff}, M_{\rm sp}^{\rm eff}\}$ are found to be negatively correlated for the former case and positively correlated for the latter. We obtain similar projected uncertainties on the cosmological parameters (in either case) for both the inflaton/moduli decay and the Dodelson-Widrow models when the first two moments of the LiMR distribution function, related to the phenomenological parameters, are matched. Finally, by constructing a modified distribution that matches the first two moments of the Dodelson-Widrow but deviates maximally in the third moment, we demonstrate that CMB Stage IV data is not expected to be sensitive to higher moments of the distribution.

DOI: 10.1103/cyq6-hnl2

I. INTRODUCTION

The cosmic microwave background (CMB) provides a snapshot of the Universe at the time of recombination—when electrons and protons combined to form hydrogen atoms—which occurred about 380,000 years after the end of inflation. Post recombination, photons decoupled from the cosmic plasma giving rise to the CMB. Likewise, neutrinos decoupled from the plasma when the expansion rate of the Universe exceeded the rate of weak interactions, when the Universe was about a second old. This gave rise to the cosmic neutrino background (CνB), which has not been detected yet, but analysis of CMB anisotropies (e.g., [1–3]) and agreement between calculated and observed primordial abundances of light elements indirectly establishes its presence [4]. An important observable in any cosmological model is the energy density in radiation at the time of recombination. Within the Standard Model (SM), photons and neutrinos are the sole contributors to this. More generally, with beyond the Standard Model (BSM) physics, there can be contributions from other species. Observational results are usually reported by making use of the quantity $N_{\rm eff}$, the effective number of neutrino like species contributing to the radiation energy density before photon decoupling, in addition to that of photons. Current constraints on $N_{\rm eff}$ from CMB measurements are 2.99 ± 0.17 (68% CL; Planck Temperature–Temperature (TT), Temperature-E(electric) mode polarization (TE), EE + lensing + BAO) [5] and $N_{\rm eff} < 3.08$ (one tail 95%; P-ACT-LB) [6], which are consistent with the SM prediction of $N_{\rm eff} = 3.044$ [7–9]. However, there is still room for $\Delta N_{\rm eff} \equiv N_{\rm eff} - 3.044 \neq 0$ once we include recent Baryon Acoustic Oscillations (BAO) measurements from Dark Energy Spectroscopic Instrument (DESI) DR2: $N_{\rm eff} = 3.10 \pm 0.17$ (68% CL; DESI + CMB) [10] and

*Contact author: abhikbhattacharjee@hri.res.in
†Contact author: rksharma@physik.rwth-aachen.de

$N_{\rm eff} = 3.23 \pm 0.18$ (68% CL; DESI BAO + CMB) [11]. So the possibility of the existence of extra relativistic particles is not ruled out yet. Furthermore, $N_{\rm eff}$ will be probed with even greater precision with future CMB experiments. For example, an experiment with the specifications of the CMB Stage IV (CMB-S4) survey will have far better sensitivity to $N_{\rm eff}$, with a target of $\sigma(N_{\rm eff}) = 0.02$–$0.03$ for the ΛCDM model extended by $N_{\rm eff}$ [12]. A quantitative understanding of possible constraints on theoretical models with the expected data quality from CMB-S4 is timely.

The presence of new light relics that behave as "dark radiation" and contribute to $\Delta N_{\rm eff}$, is a generic feature of many BSM proposals. Sources for dark radiation include sterile neutrinos (e.g., [13–15]) and axions (e.g., [16–22]), among others.[1] Certain studies propose the existence of sterile neutrinos [23–25] to address anomalies in neutrino oscillation data [26,27]. In spite of the particle physics motivation, a fully thermalized fourth sterile neutrino that decoupled along with the standard neutrinos is ruled out due to stringent constraints on $N_{\rm eff}$ mentioned above [5]. Models with more complicated structures for the neutrino sector have also been proposed (e.g., [28]), and possible constraints from cosmological data have been investigated [29]. However, hot thermal relics that decoupled from the SM plasma at an earlier time than neutrino decoupling could be exempted from the strong constraints on $N_{\rm eff}$. Thermal relics with decoupling temperatures above the top quark mass have the following minimal contributions: $\Delta N_{\rm eff} = 0.027$ for a Goldstone boson, $\Delta N_{\rm eff} = 0.047$ for a Weyl fermion, and $\Delta N_{\rm eff} = 0.054$ for a vector boson [30]. The cosmological impact of such massless light relics (or relics with masses $m \ll$ eV) is completely captured by the $N_{\rm eff}$ parameter [17]. They primarily affect the expansion of the Universe, causing a suppression of the damping tail of the CMB power spectrum as well as a phase shift in the baryon acoustic oscillations [1,17,20,31,32].

The other possibility is that of light massive relics (LiMRs)—massive particles that contributed to the radiation energy density in the early Universe and to the matter energy density at late times. The LiMR mass is an important parameter as it controls the time at which the LiMR transitions to being nonrelativistic, after which it behaves as a subcomponent of the total dark matter (DM) component of the Universe. Increasing the effective mass of the LiMR primarily affects the CMB power spectrum at low multipoles through the late Integrated Sachs-Wolfe (ISW) effect and CMB lensing [4,33,34]. In Ref. [35], the authors combined CMB and LSS data to obtain limits on the masses of thermally decoupled species X [with a present day temperature of $T_X^{(0)} = 0.91$ K]: $m_X \leq 11, 2.3, 1.6$ eV for scalars, Weyl fermions, and vectors, respectively. Fisher forecasts for such LiMRs, with masses ranging from 10^{-2} eV $\leq m_X \leq 10$ eV and temperatures in the range $[0.91\ \text{K}, 1.50\ \text{K}]$, have been performed in Ref. [36] to predict constraints on g_X, the number of degrees of freedom of the LiMR, from the CMB-S4 experiment.

While much of the literature has focused on thermal relics, this paper deals with LiMRs in *nonthermal* distributions. Various well-motivated models have been proposed to generate species with nonthermal distributions in the early Universe. One of the familiar categories is through mixing of active neutrinos [37,38], while another is through the decay of heavy particles in the early Universe [39–44]. Belonging to the latter category is the perturbative decay of the inflaton [45] or the decay of the moduli due to vacuum misalignment (see, for instance, Ref. [46]). We focus on two concrete examples of such distributions to draw out the main features: the first arises from the inflaton/moduli decay in the early Universe (e.g., [40,43]). The second distribution we examine is the Dodelson-Widrow distribution [37,47], originally proposed for sterile neutrinos. We perform Fisher forecasts for these models to quantify the expected uncertainties on their parameters that are expected from a survey with the specifications of the CMB-S4 experiment.[2] We also investigate how features of the shape of the LiMR distribution function can affect observables.

The paper is structured as follows: Sec. II gives a brief review of some basic aspects of the LiMR models, Fisher forecasts, and future experimental prospect. We discuss our implementation in Sec. III. Our results are presented in Sec. IV. In Sec. V, we discuss the effect of the shape of the distribution function. We conclude in Sec. VI.

II. REVIEW

A. Light massive relics

We begin by discussing some general aspects of LiMR models. The influence of LiMRs on linear cosmological observables can be characterized by three parameters (see Ref. [47] for details).

(i) $\Delta N_{\rm eff}$: This parameter represents the contribution of LiMRs to the Universe's relativistic energy density before photon decoupling. It is defined as (g_s is a degeneracy factor),

$$\Delta N_{\rm eff} \equiv \frac{\rho_{\rm sp}^{\rm rel}}{\rho_\nu} = \frac{g_s}{7/4}\left[\frac{1}{\pi^2}\int dp p^3 \hat{f}(p)\right] \Big/ \left[\frac{7\pi^2}{120}(T_\nu^{\rm id})^4\right], \tag{1}$$

[1]See Ref. [12] (and references therein) for discussion of other possibilities and their prospects for detection by the CMB-S4 experiment.

[2]The preparation of this manuscript was completed before the descoping of the CMB-S4 project. Since then, we have revised the manuscript and included forecasts for a cosmic variance–limited experiment in addition to those of a CMB-S4–like experiment. We have also included forecasts for the Simons Observatory-Large Aperture Telescope (SO-LAT) in Sec. IV.

where $\hat{f}(p)$ is the momentum distribution function of the LiMR, and $T_\nu^{\rm id} \equiv (4/11)^{1/3} T_\gamma$ is the neutrino temperature in terms of the photon temperature, assuming instantaneous neutrino decoupling.

(ii) $M_{\rm sp}^{\rm eff}$: This parameter represents the contribution of the LiMR to the Universe's current energy density, and it is defined as (g_s' is a degeneracy factor),

$$\frac{M_{\rm sp}^{\rm eff}}{94.05\ {\rm eV}} \equiv \omega_{\rm sp} = \frac{g_s'}{3/2}\left[\frac{m_{\rm sp}}{\pi^2}\int dp p^2 \hat{f}(p)\right]\left[\frac{h^2}{\rho_{\rm crit}^0}\right], \tag{2}$$

where h is the reduced Hubble constant and $\rho_{\rm crit}^0$ denotes the critical density of the Universe today.

(iii) $\langle v_{\rm fs}\rangle$: The typical free-streaming velocity of the particles today, given by

$$\langle v_{\rm fs}\rangle \equiv \frac{\frac{g_s}{7/4}\int dp p^2 \frac{p}{m_{\rm sp}}\hat{f}(p)}{\frac{g_s'}{3/2}\int dp p^2 \hat{f}(p)} = 5.236\times 10^{-4}\frac{\Delta N_{\rm eff}}{M_{\rm sp}^{\rm eff}}. \tag{3}$$

Note that only two of the three parameters are independent. In our study, we will utilize $M_{\rm sp}^{\rm eff}$ and $\Delta N_{\rm eff}$ as phenomenological parameters to investigate the impact of LiMRs. Also, the above described parameters are determined by the first two moments of the distribution function. We will examine the role of higher moments in Sec. V. Note that the parameter g_X of Ref. [35] is related to our g_s, g_s'. But unlike in Ref. [35], where the uncertainties on $\Delta N_{\rm eff}$ or $M_{\rm sp}^{\rm eff}$ (equivalently Ω_X) were obtained by translating the predicted uncertainty on g_X, here we shall find the uncertainties on these phenomenological parameters by varying the mass $m_{\rm sp}$ and a model specific parameter (see below), which enters into the momentum distribution function.

Next, we describe the two LiMR distribution functions that we will consider in the paper.

1. Distribution function associated with production via decay of the inflaton/moduli

During reheating after inflation or an epoch of moduli domination, the early Universe can go through a matter-dominated era with its energy density dominated by heavy cold particles (ϕ). In addition to the decay to the SM sector, the ϕ particle can decay to a LiMR in the dark sector. This typically occurs via a $1\to 2$ process,

$$\phi \xrightarrow{B_{\rm sp}} {\rm xx},$$

where x stands for the LiMR.[3] The production rate of x is controlled by the decay lifetime τ, the mass m_ϕ, and the branching ratio $B_{\rm sp}$. LiMRs produced via this mechanism have the following momentum distribution (as given in Ref. [43]; see Appendix A for further details):

$$f(\boldsymbol{q}) = \frac{32}{\pi \hat{E}^3}\left(\frac{N(0)B_{\rm sp}}{\hat{s}^3(\theta^*)}\right)\frac{\exp\left(-\hat{s}^{-1}(y)\right)}{|\boldsymbol{q}|^3 \hat{H}(\hat{s}^{-1}(y))}. \tag{4}$$

Here $\hat{E}$ is the energy of the particles at production, $N(0)$ is the initial number density of the ϕ particles, $\hat{s}(\theta)\equiv a(t)$ is the scale factor as a function of dimensionless time θ (with θ^* indicating the time by which all the ϕ particles have decayed), $\hat{s}^{-1}$ is the functional inverse of the scale factor function, and $\hat{H} = \hat{s}'(\theta)/\hat{s}(\theta)$ is the dimensionless Hubble parameter. The argument of the distribution function is $\boldsymbol{q} \equiv \boldsymbol{p}/T_{\rm ncdm,0}$ where $T_{\rm ncdm,0}$ is the typical momentum of the LiMRs today. Motivated by the expectation that most ϕ particles decay well before θ^*, the authors in Ref. [43] took $T_{\rm ncdm,0} = \frac{\hat{E}}{4}\frac{a(t^*)}{a(t_0)}$, which leads to the following constraint on $|\boldsymbol{q}|$, when coupled with Eq. (A8),

$$\frac{4}{\hat{s}(\theta^*)} < |\boldsymbol{q}| < 4. \tag{5}$$

The model has four microscopic parameters: $m_\phi, \tau, B_{\rm sp}$, and $m_{\rm sp}$. We will take the first two parameters to be $m_\phi \sim 10^{-6} M_{\rm Pl}$ and $\tau \sim 10^8/m_\phi$ (motivated by having ϕ to be driving inflation at the GUT scale and decaying by GUT scale interactions). The phenomenological parameters $\{\Delta N_{\rm eff}, M_{\rm sp}^{\rm eff}\}$ are related to the model parameters by the following expressions [43]:

$$\Delta N_{\rm eff} = \frac{43}{7}\frac{B_{\rm sp}}{1-B_{\rm sp}}\left(\frac{g_*(T(t_\nu))}{g_*(T(t^*))}\right)^{1/3}, \tag{6}$$

$$M_{\rm sp}^{\rm eff} = \frac{62.1 m_{\rm sp}}{g_*^{1/4}(T(t^*))}\frac{B_{\rm sp}}{(1-B_{\rm sp})^{3/4}}\left(\frac{M_{\rm Pl}}{\tau m_\phi^2}\right)^{1/2}, \tag{7}$$

where t_ν is the neutrino-decoupling time and $g_*(T(t))$ is the effective number of degrees of freedom at a temperature T (corresponding to a time t).

[3]Here x behaves as a hot/warm dark matter candidate. Cold dark matter production in an early matter-dominated era (EMDE) has also been studied, for instance, in Refs. [48,49]. Several other works have also examined how an EMDE modifies dark-matter production, cosmological evolution, and particle constraints, including studies of ultracold Weakly Interacting Massive Particles (WIMPs), gravitational heating, freeze-in and freeze-out during EMDEs, 21-cm signatures, and related nonstandard thermal histories [50–62]. Also see Ref. [63] for a minireview of thermal and nonthermal DM production in nonstandard cosmologies.

2. The Dodelson-Widrow distribution

We also consider the Dodelson-Widrow distribution [37]. Nonresonant active-sterile neutrino oscillations in the early Universe in the limit of small mixing angle and zero leptonic asymmetry leads to the following distribution function for the sterile neutrinos [47]:

$$f_\nu(p) = \frac{\chi}{e^{p/T_\nu} + 1}, \tag{8}$$

where χ is an arbitrary normalization factor and T_ν is the temperature of neutrinos today. With $T_\nu = T_\nu^{\rm id}$, the phenomenological parameters are related to the model parameters via the following relations:

$$\Delta N_{\rm eff} = \chi \quad \text{and} \quad M_{\rm sp}^{\rm eff} = m_{\rm sp} \times \chi, \tag{9}$$

where $m_{\rm sp}$ is the mass of the sterile neutrinos.

B. Fisher forecast methodology

1. Formalism

Suppose we have a set of data $\{\boldsymbol{d}\}$ and a model $\mathcal{M}$ with a set of parameters $\{\boldsymbol{\theta}\}$. We want to find the probability distribution of $\{\boldsymbol{\theta}\}$, given the data $\{\boldsymbol{d}\}$, i.e., $P(\boldsymbol{\theta}|\boldsymbol{d})$, which is obtained using Bayes's theorem,

$$P(\boldsymbol{\theta}|\boldsymbol{d}) \propto P(\boldsymbol{d}|\boldsymbol{\theta})P(\boldsymbol{\theta}). \tag{10}$$

Here $P(\boldsymbol{\theta})$ and $P(\boldsymbol{\theta}|\boldsymbol{d})$ are called the *prior* and *posterior* distributions, respectively, and $P(\boldsymbol{d}|\boldsymbol{\theta})$ is called the *likelihood*, usually denoted by $\mathcal{L}$, and can be expressed as follows [64]:

$$\mathcal{L}(\boldsymbol{d};\boldsymbol{\theta}) = \frac{1}{\sqrt{(2\pi)^n |\mathbf{C}(\boldsymbol{\theta})|}} \exp\left(-\frac{1}{2}\boldsymbol{d}^T \mathbf{C}(\boldsymbol{\theta})\boldsymbol{d}\right), \tag{11}$$

where $\mathbf{C}$ represents the covariance matrix and n is the dimension of the data vector $\boldsymbol{d}$. The Fisher matrix is related to the curvature of the log-likelihood function, evaluated at the fiducial values of the parameters,

$$F_{ij} = -\left\langle \frac{\partial^2 \ln \mathcal{L}}{\partial\theta_i \partial\theta_j} \right\rangle \Bigg|_{\boldsymbol{\theta}=\boldsymbol{\theta}_0}, \tag{12}$$

θ_i, θ_j being the parameters of interest and $\boldsymbol{\theta}_0$ being the fiducial set of parameters [65]. *Derived parameters.* If we have a Fisher matrix in terms of a set of parameters $\{\boldsymbol{\theta}\}$, we can obtain a new Fisher matrix in terms of a set of derived parameters $\{\boldsymbol{\theta}'\}$ as [66]

$$F' = J^T \cdot F \cdot J, \tag{13}$$

where J stands for the inverse Jacobian matrix $\partial\boldsymbol{\theta}/\partial\boldsymbol{\theta}'$. This will be used, for instance, to translate the 1σ uncertainties on $\{B_{\rm sp}, m_{\rm sp}\}$ to those on $\{\Delta N_{\rm eff}, M_{\rm sp}^{\rm eff}\}$.

Error estimate. After computing the Fisher information matrix, we can derive the error covariance matrix by taking its inverse

$$\mathrm{Cov}_{ij} = (F^{-1})_{ij}. \tag{14}$$

The diagonal elements of the error covariance matrix indicate the marginalized errors on the parameters. For instance, the anticipated marginalized 1σ error on a parameter θ_i, accounting for all degeneracies concerning other parameters, is calculated as,

$$\sigma_i^{(\rm marg.)} = \sqrt{\mathrm{Cov}_{ii}}. \tag{15}$$

The unmarginalized expected errors, or conditional errors, can be determined by

$$\sigma_i^{(\rm cond.)} = \sqrt{\frac{1}{F_{ii}}}, \tag{16}$$

representing the square root of the reciprocal of the relevant diagonal element of the Fisher matrix.

Posterior probability or confidence regions. For the form of the likelihood function (11), the posterior probability is Gaussian (under the Fisher assumption[4]) with the 1σ and 2σ intervals encompassing 68.3% and 95.4% of the total probability, respectively. For Gaussian posterior, the confidence regions are ellipses in the parameter space, whose size and orientation are determined by the Fisher matrix elements. Confidence regions correspond to regions in parameter space in which the joint parameter values are expected to lie with a certain probability—1σ region corresponds to 39.35% probability and 2σ region corresponds to 86.47% probability.

2. CMB experiments

In the context of CMB, the data vector is either the CMB power spectra or spherical harmonic coefficients represented as $\boldsymbol{d} = \{a_{\ell m}^T, a_{\ell m}^E, a_{\ell m}^\phi\}$. The Fisher information matrix takes the following form [67]:

$$F_{ij} = \sum_\ell \frac{2\ell+1}{2} f_{\rm sky} \mathrm{Tr}\left(\mathbf{C}_\ell^{-1}(\boldsymbol{\theta}) \frac{\partial \mathbf{C}_\ell}{\partial\theta_i} \mathbf{C}_\ell^{-1}(\boldsymbol{\theta}) \frac{\partial \mathbf{C}_\ell}{\partial\theta_j}\right), \tag{17}$$

where $f_{\rm sky}$ is the fractional sky coverage, $\boldsymbol{\theta}$ represents the vector of parameters, and $\mathbf{C}_\ell$ is the total covariance matrix of the relevant CMB observables (temperature, E-mode polarization, and lensing potential) given by [68],

$$\mathbf{C}_\ell = \begin{pmatrix} C_\ell^{TT} + N_\ell^{TT} & C_\ell^{TE} & C_\ell^{T\phi} \\ C_\ell^{TE} & C_\ell^{EE} + N_\ell^{EE} & 0 \\ C_\ell^{T\phi} & 0 & C_\ell^{\phi\phi} + N_\ell^{\phi\phi} \end{pmatrix}.$$

[4]One can have non-Gaussian posteriors in general even for a Gaussian likelihood when priors are non-Gaussian.

TABLE I. Experimental parameters for Planck, SO-LAT, and a particular configuration of the CMB-S4 experiment used for the Fisher analysis. We also considered a stand-alone, full-sky, cosmic-variance limited experiment.

Experiment	ℓ range	Noise $s[\mu\mathrm{K}-\mathrm{arcmin}]$	f_{sky}	θ_{FWHM} [arcmin]
Planck	T: 2–2500 P: 30–2500	T: [145, 149, 137, 65, 43, 66, 200] P: [−, −, 450, 103, 81, 134, 406]	0.6	[33, 23, 14, 10, 7, 5, 5]
SO-LAT	T: 30–3000 P: 30–5000	T: [61, 30, 5.3, 6.6, 15, 35] P: [86.2, 42.4, 7.5, 9.3, 21.2, 49.5]	0.4	[7.4, 5.1, 2.2, 1.4, 1.0, 0.9]
CMB-S4	T: 30–3000 P: 30–5000	T: 1.0 P: 1.414	0.4	1.5
CV-limited	T/P: 2–5000	0.0	1.0	N/A

This includes the Gaussian noise N_ℓ^{XX}, where $XX \in \{TT, EE\}$, given by [12]

$$N_\ell^{XX} = s^2 \exp\left(\ell(\ell+1)\frac{\theta^2_{\mathrm{FWHM}}}{8\ln 2}\right), \tag{18}$$

where θ_{FWHM} is the resolution of the experiment in arcmin, and s is the instrumental noise in temperature/polarization.

III. IMPLEMENTATION

The C_ℓ's appearing in the total covariance matrix $\mathbf{C}_\ell$ above were obtained from the publicly available package CLASS[5] [69], suitably modified to incorporate the non-thermal distribution functions under consideration [70]. The noise properties for the experiments considered in this work are listed in Table I [12,71,72], and the TT and Electric-Electric mode polarization (EE) noise spectra were computed using Eq. (18) with these noise parameters. For the lensing convergence, we used the ORPHICS[6] code [73] to calculate the noise spectrum $N_\ell^{\kappa\kappa}$ (subsequently converted to $N_\ell^{\phi\phi}$) from a minimum variance combination of TT, TE, EE, EB, and TB quadratic estimators, assuming the CMB B modes undergo an iterative delensing procedure. Following the CMB-S4 Science Book [12] and the Simons Observatory Science Book [74], we have set $\ell_{\mathrm{min}} = 30$ (recovering large scales from the ground is challenging), and $\ell^T_{\mathrm{max}} = 3000$ and $\ell^P_{\mathrm{max}} = 5000$ for CMB-S4 and SO-LAT (due to foregrounds). For Planck, we have considered $2 < \ell^T < 2500$ and $30 < \ell^P < 2500$. For the lensing signal, we have considered $30 < \ell^\phi < 2500$. We have assumed infinite noise outside these multipole ranges [71] and have set the derivatives of the C_ℓ's to zero outside the corresponding multipole ranges to ignore their contribution to our analysis.[7] When analyzing $C_\ell^{TT}, C_\ell^{TE}, C_\ell^{EE}$ in combination with the lensing convergence spectra $C_\ell^{\phi\phi}$ (which has been assumed to contain all the lensing information), we have used unlensed C_ℓ's in our Fisher analysis in order to avoid double-counting lensing information [71].

Measurements of CMB-S4/SO are usually considered in combination with Planck data because the two experiments are highly complementary. Planck, as a satellite mission, provides a higher sky coverage and can also capture the largest angular scales (low ℓ's). On the other hand, CMB-S4/SO, being a ground-based experiment offers better sensitivity and precision on smaller angular scales (high ℓ's). So for the Planck and CMB-S4/SO joint analysis, we added the corresponding Fisher matrices,

$$F = F^{\mathrm{Planck}} + F^{\mathrm{CMB\text{-}S4/SO}}, \tag{19}$$

with the caveat that in the region of overlap between the two experiments, which is $30 < \ell < 2500$, we set $f_{\mathrm{sky}} = 0.2$ for Planck in order to avoid double counting [71]. When considering SO in combination with Planck, we set $f_{\mathrm{sky}} = 0.8$ for Planck for $2 < \ell < 30$ [74]. We used flat priors for all parameters except τ_{reio}, for which we have added a prior of 0.01 as follows [75]:

$$F_{ii} \to F_{ii} + \frac{1}{\mathrm{prior}_i^2}. \tag{20}$$

We utilized the FISHCHIPS package[8] to develop our code for Fisher analysis.

IV. RESULTS

The fiducial model consists of the following six ΛCDM parameters: the physical baryon density ω_b, the physical cold dark matter density ω_{cdm}, the reduced Hubble constant h, the amplitude of primordial scalar perturbations A_s, the scalar spectral tilt n_s, and the optical depth to reionization τ_{reio}, and the two phenomenological parameters $\{\Delta N_{\mathrm{eff}}, M_{\mathrm{sp}}^{\mathrm{eff}}\}$. The phenomenological parameters are however derived parameters—related to the

[5] https://github.com/lesgourg/class-public
[6] https://github.com/msyriac/orphics
[7] See Appendix B for a discussion on numerical derivatives.
[8] https://github.com/xzackli/fishchips-public

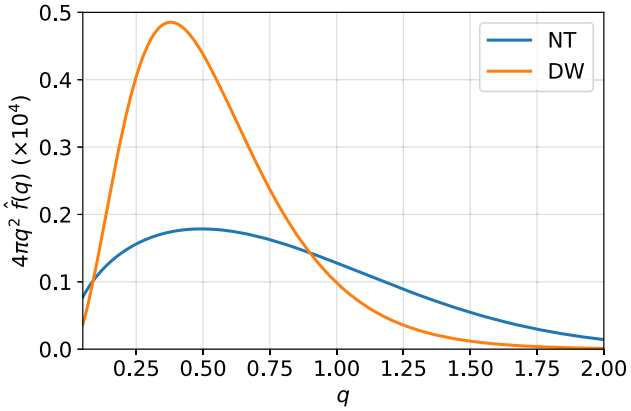

FIG. 1. Comparative plot of the inflaton decay (NT) and DW distributions for $\{\Delta N_{\rm eff}, M_{\rm sp}^{\rm eff}\} = \{0.034, 0.903\ {\rm eV}\}$. The momenta and the distribution function are both in units of $T_{\rm ncdm,0}$ which is calculated using Eq. (A11) with $m_\phi = 10^{-6} M_{\rm Pl}$, $\tau = 10^8/m_\phi$, and $B_{\rm sp} = 0.0118$ for the NT model.

inflaton/moduli-decay-model parameters $\{B_{\rm sp}, m_{\rm sp}\}$ [via Eqs. (6) and (7)] or the Dodelson-Widrow-model parameters $\{\chi, m_{\rm sp}\}$ [via Eq. (9)]. For both these models, we assume Standard Model neutrinos to be massless as in Ref. [76], since the effect of neutrino masses is expected to be subdominant for the cosmological observables of interest. In Fig. 1, we plot the nonthermal (NT) distribution along with the Dodelson-Widrow (DW) distribution for the same values of the phenomenological parameters, viz. $\Delta N_{\rm eff} = 0.034$ and $M_{\rm sp}^{\rm eff} = 0.903$ eV.

We have performed the Fisher analyses with two sets of fiducial values:

(i) Set I: We used the best fit of Markov-Chain-Monte-Carlo (MCMC) analysis with Planck 18 +S8 datasets performed in Ref. [76] for the inflaton decay model. The fiducial values of the $\nu_{\rm NT}\Lambda$CDM model parameters, corresponding to the fiducial values of the phenomenological parameters, $\{\Delta N_{\rm eff}, M_{\rm sp}^{\rm eff}\} = \{0.034, 0.903\ {\rm eV}\}$, are

$$B_{\rm sp} = 0.0118, \qquad m_{\rm sp} = 38.62\ {\rm eV}, \tag{21}$$

whereas for the Dodelson-Widrow model, we have

$$\chi = 0.034, \qquad m_{\rm sp} = 26.43\ {\rm eV}. \tag{22}$$

(ii) Set II: We used the mean values of the ΛCDM parameters obtained from Planck TT, TE, EE+low E + lensing when the base-ΛCDM model is extended by including $M_{\rm sp}^{\rm eff}$ and $N_{\rm eff}$ [5]. In this extension of the base ΛCDM model, the physical mass of a thermal sterile neutrino is $m_{\rm sp}^{\rm th} = (\Delta N_{\rm eff})^{-3/4} M_{\rm sp}^{\rm eff}$. Assuming the prior $m_{\rm sp}^{\rm th} < 10$ eV, the Planck-2018 paper found the following 2σ constraints on $\Delta N_{\rm eff}$ and $M_{\rm sp}^{\rm eff}$ from Planck TT, TE, EE + low E + lensing + BAO:

$$\Delta N_{\rm eff} < 0.246 \quad \text{and} \quad M_{\rm sp}^{\rm eff} < 0.65\ {\rm eV}. \tag{23}$$

We chose $\Delta N_{\rm eff} = 0.1$ and $M_{\rm sp}^{\rm eff} = 0.415$ eV, which corresponds to the following values of the model parameters:

$$B_{\rm sp} = 0.0332, \qquad m_{\rm sp} = 6.20\ {\rm eV}; \tag{24}$$

$$\chi = 0.1, \qquad m_{\rm sp} = 4.15\ {\rm eV}. \tag{25}$$

We emphasize that both fiducial sets correspond to the same phenomenological parametrization; they are simply two benchmarks representing different parts of the parameter space—a heavier particle with a smaller contribution to $\Delta N_{\rm eff}$ (set I) and a lighter particle with a higher contribution to $\Delta N_{\rm eff}$ (set II). The fiducial values of the ΛCDM parameters along with the phenomenological parameters $\{\Delta N_{\rm eff}, M_{\rm sp}^{\rm eff}\}$ are listed in Table II.

TABLE II. Fiducial values used for Fisher analysis.

Parameter	Fiducial value	
	Set I	Set II
ω_b	0.02247	0.02242
$\omega_{\rm cdm}$	0.111	0.120
h	0.6804	0.6711
$10^9 A_s$	2.099	2.110
n_s	0.9661	0.9652
$\tau_{\rm reio}$	0.0536	0.0560
$\Delta N_{\rm eff}$	0.034	0.1
$M_{\rm sp}^{\rm eff}$ [eV]	0.903	0.415

Various autocorrelation spectra obtained from CLASS (and ORPHICS) using the parameter values of set I for the inflaton/moduli decay model are plotted in Fig. 2, which also shows the improvements in the noise levels for CMB-S4/SO as compared to Planck. In Fig. 3 we show the comparative plots of C_ℓ^{TT}, C_ℓ^{EE}, and $C_\ell^{\phi\phi}$ for the two sets of fiducial values for the NT model. More $\Delta N_{\rm eff}$ leads to more damping of the primary CMB spectra at higher ℓ. Although the free-streaming velocity of the LiMR is more in the case of set II, the suppression of the lensing spectrum $C_\ell^{\phi\phi}$ is less compared to set I. This is because, in set I, the CDM component is reduced at the cost of the LiMR component. The net effect is less clustering power and hence greater suppression of $C_\ell^{\phi\phi}$. For set II, structure grows more efficiently, despite the fact that $\langle v_{\rm fs}\rangle$ is roughly ten times greater than that for set I, leading to stronger lensing potentials and hence $C_\ell^{\phi\phi}$ is less suppressed. We will restrict our analyses to the linear regime since nonlinear matter power spectrum corrections (via HALOFIT or HMCODE) are not appropriate for models where the dark

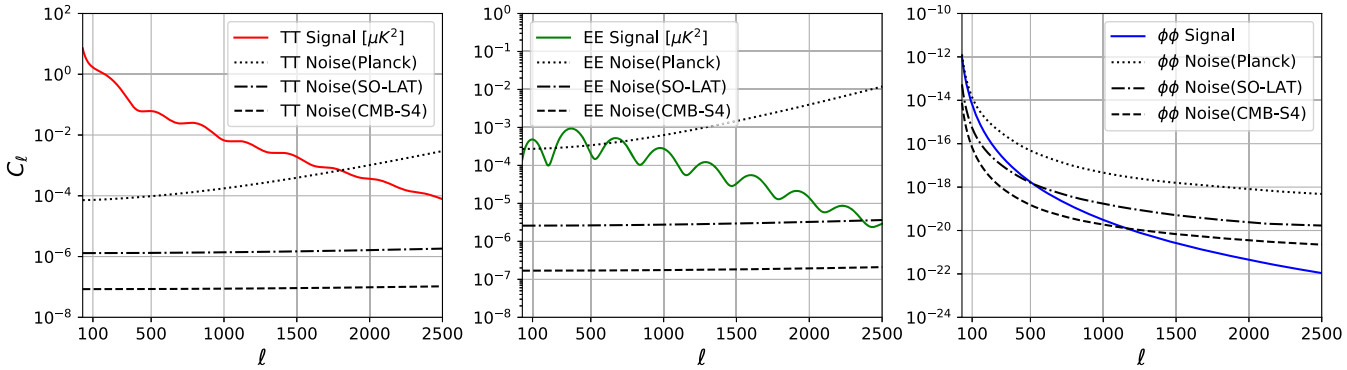

FIG. 2. Plots of various autocorrelation signal and noise spectra for the inflaton/moduli decay model with the parameter values from Table II (set I).

sector includes massive hot dark matter or warm dark matter components.

Before analyzing these two sets, as a preliminarily study, we will compare the two nonthermal models, with the LiMR masses fixed to zero, with the ΛCDM model extended by the $N_{\rm eff}$ parameter, which we will refer to as the $\nu\Lambda$CDM model. We will perform the Fisher analysis by marginalizing over the six ΛCDM parameters, along with $N_{\rm eff}$ for the $\nu\Lambda$CDM model, or $B_{\rm sp}$ for the NT model, or χ for the DW model, in order to find the projected uncertainties on $N_{\rm eff}$ around $\Delta N_{\rm eff} = 0$. To this end, we use the following fiducial values for the seventh parameter: $N_{\rm eff} = 0$, $B_{\rm sp} = 0$, and $\chi = 0$ for the $\nu\Lambda$CDM model, the NT model, and the DW model, respectively.[9] We use the following fiducial values for the ΛCDM model parameters [5]: $\omega_b = 0.02224, \omega_{\rm cdm} = 0.1179, h = 0.663$, $A_s = 2.082 \times 10^{-9}, n_s = 0.9589$, and $\tau_{\rm reio} = 0.05$. The 1σ projected uncertainties on $N_{\rm eff}$ from CMB-S4 were found to be as follows:

$$\sigma(N_{\rm eff}) = \begin{cases} 0.028 & (\nu\Lambda\text{CDM}) \\ 0.025 & (\text{NT}) \\ 0.029 & (\text{DW}) \end{cases} . \qquad (26)$$

The fact that our forecasts for these three models (when expanding around the same fiducial cosmology) are in line with each other is consistent with the expectation that these models would be indistinguishable since they have the same phenomenological parameters $\Delta N_{\rm eff} \approx 0$ and $M_{\rm sp}^{\rm eff} = 0$ eV.

A. Forecasts for inflaton-decay nonthermal and Dodelson-Widrow models

Now we move on to the results of the Fisher forecasts for the LiMRs with the fiducial values in Table II.

[9]For the numerical implementation, we set $B_{\rm sp} = 10^{-6}$ and $\chi = 2.92 \times 10^{-6}$.

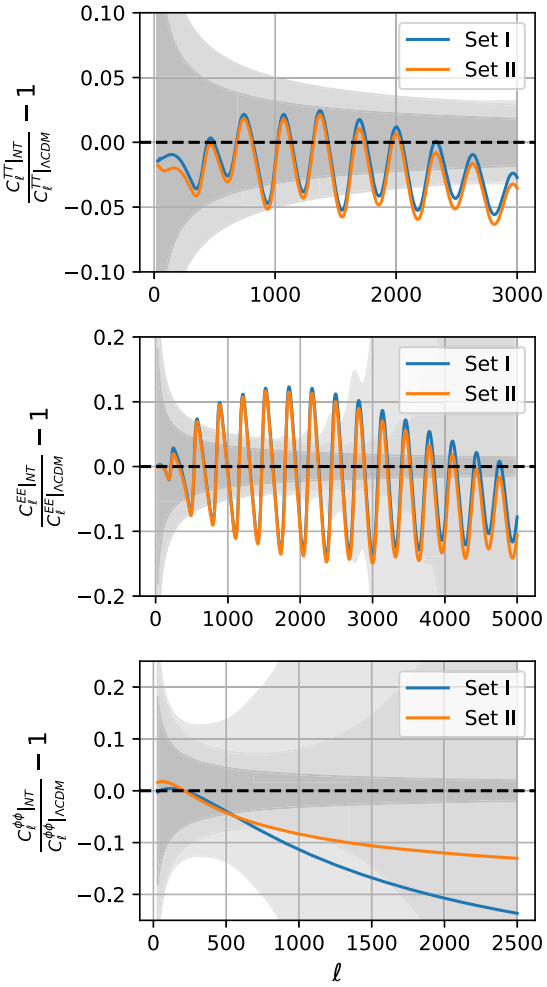

FIG. 3. Comparison of the residuals of the TT, EE, and $\phi\phi$ spectra for the two sets of fiducial values. The progressively darker shaded regions correspond respectively to the 1σ error bars associated with the particular configurations of the SO-LAT experiment, the CMB-S4 experiment, and to the CV-limited experiment considered in this work (see Table I).

TABLE III. Projected 1σ errors for parameters θ_i, marginalized over all other parameters for the inflaton-decay NT model with $\{\Delta N_{\rm eff}, M_{\rm sp}^{\rm eff}\} = \{0.034, 0.903\ {\rm eV}\}$ (set I).

Parameter	$10^5\omega_b$	$10^3\omega_{\rm cdm}$	H_0	$\ln(10^{10}A_s)$	n_s	$\tau_{\rm reio}$	$\Delta N_{\rm eff}$	$M_{\rm sp}^{\rm eff}$ [eV]
1σ error (SO)	4.20	3.11	0.301	0.011	0.0022	0.0064	0.0061	0.249
1σ error (Planck + SO)	3.99	3.05	0.281	0.011	0.0019	0.0061	0.0059	0.247
1σ error (CMB-S4)	2.84	1.29	0.270	0.010	0.0020	0.0059	0.0039	0.081
1σ error (Planck + S4)	2.74	1.25	0.254	0.010	0.0019	0.0057	0.0038	0.080
1σ error (CV limited)	0.798	0.302	0.092	0.0026	0.0008	0.0014	0.0013	0.0119

TABLE IV. Same as Table III with $\{\Delta N_{\rm eff}, M_{\rm sp}^{\rm eff}\} = \{0.1, 0.415\ {\rm eV}\}$ (set II).

Parameter	$10^5\omega_b$	$10^3\omega_{\rm cdm}$	H_0	$\ln(10^{10}A_s)$	n_s	$\tau_{\rm reio}$	$\Delta N_{\rm eff}$	$M_{\rm sp}^{\rm eff}$ (eV)
1σ error (SO)	5.07	1.42	0.322	0.014	0.0029	0.0072	0.039	0.049
1σ error (Planck + SO)	4.95	1.34	0.299	0.013	0.0026	0.0069	0.037	0.047
1σ error (CMB-S4)	3.53	1.04	0.285	0.013	0.0024	0.0067	0.030	0.028
1σ error (Planck + S4)	3.47	0.99	0.267	0.012	0.0023	0.0065	0.029	0.026
1σ error (CV limited)	0.978	0.277	0.093	0.0028	0.0008	0.0015	0.0066	0.0091

TABLE V. Comparison of the projected 1σ errors from CMB-S4 for parameters θ_i, marginalized over all other parameters for the NT and DW models.

	Model	$10^5\omega_b$	$10^3\omega_{\rm cdm}$	H_0	$\ln(10^{10}A_s)$	n_s	$\tau_{\rm reio}$	$\Delta N_{\rm eff}$	$M_{\rm sp}^{\rm eff}$ (eV)
Set I	NT	2.85	1.26	0.263	0.010	0.0019	0.0059	0.0038	0.080
	DW	2.85	1.17	0.266	0.010	0.0020	0.0059	0.0034	0.073
Set II	NT	3.53	1.03	0.285	0.013	0.0024	0.0067	0.030	0.028
	DW	3.73	1.04	0.295	0.013	0.0026	0.0071	0.031	0.030

(i) Set I: The projected 1σ uncertainties on the fiducial model parameters are reported in Table III. The Fisher ellipses for the parameters $\{\omega_m = \omega_b + \omega_{\rm cdm}, h, \Delta N_{\rm eff}, M_{\rm sp}^{\rm eff}\}$ are shown in Fig. 4(a). As expected, combined analysis of Planck and CMB-S4/SO leads to tighter constraints on the parameters. From Table V, one can see that the NT model and the DW model uncertainties are in close agreement with each other. Of our particular interest are the phenomenological parameters, whose 1σ uncertainties from CMB-S4 + Planck are

$$1\sigma(\Delta N_{\rm eff}) = \begin{cases} 0.0038 & ({\rm NT}) \\ 0.0033 & ({\rm DW}) \end{cases}, \tag{27}$$

and

$$1\sigma(M_{\rm sp}^{\rm eff}) = \begin{cases} 80\ {\rm meV} & ({\rm NT}) \\ 76\ {\rm meV} & ({\rm DW}) \end{cases}. \tag{28}$$

(ii) Set II: The Fisher plots are shown in Fig. 4(b) and the 1σ uncertainties are given in Table IV. We again see from Table V that the DW model parameter uncertainties agree quite well with the corresponding uncertainties for the NT model. With this set of fiducial values, we obtain the following 1σ uncertainties from CMB-S4 + Planck,

$$1\sigma(\Delta N_{\rm eff}) = \begin{cases} 0.029 & ({\rm NT}) \\ 0.030 & ({\rm DW}) \end{cases}, \tag{29}$$

and

$$1\sigma(M_{\rm sp}^{\rm eff}) = \begin{cases} 26\ {\rm meV} & ({\rm NT}) \\ 29\ {\rm meV} & ({\rm DW}) \end{cases}. \tag{30}$$

We see that the relative uncertainties on $M_{\rm sp}^{\rm eff}$ are 8.9%(8.3%) and 6.3%(7%), whereas the relative uncertainties on $\Delta N_{\rm eff}$ are 11.2%(9.7%) and 29%(30%), for the NT(DW) model. So the relative uncertainties on $M_{\rm sp}^{\rm eff}$ slightly worsen while there is a significant improvement in the relative uncertainties on $\Delta N_{\rm eff}$ in going from set II to set I. Note that the Fisher analysis has been implemented via the fundamental parametrization—$\{B_{\rm sp}, m_{\rm sp}\}$ for the NT model and $\{\chi, m_{\rm sp}\}$ for the DW model—and then projected uncertainties have been translated to those on the phenomenological parameters [using Eq. (13)].

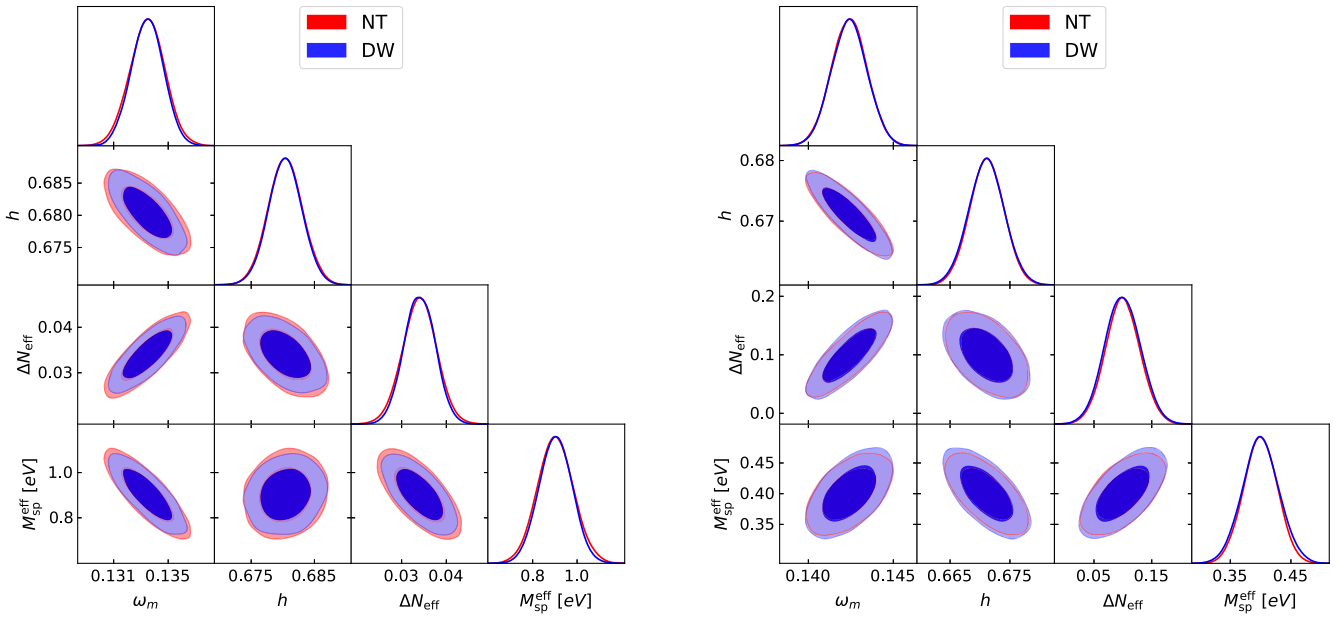

(a) (b)

FIG. 4. Posterior distributions and Fisher ellipses for the parameters $\{\omega_m = \omega_b + \omega_{\rm cdm}, h, \Delta N_{\rm eff}, M_{\rm sp}^{\rm eff}\}$ (plotted using GETDIST) for the CMB-S4 experiment. (a) Fisher plots for the NT and DW models with fiducial values set I. (b) Same as (a) with fiducial values set II.

In Figs. 5 and 6 we compare the Fisher ellipses and the posterior distributions obtained from the CMB-S4, and SO-LAT for the two sets of parameters considered in the text.

B. Discussion

Our results reveal the following noteworthy features pertaining to the phenomenological parameters.

(i) There is significant difference in the relative uncertainties on $\Delta N_{\rm eff}$ for the two sets analyzed [as seen in Eqs. (27) and (29)].

(ii) The phenomenological parameters, $\Delta N_{\rm eff}$ and $M_{\rm sp}^{\rm eff}$, are negatively correlated for the heavier particle but positively correlated for the lighter one.

In this Section, we will discuss these features and provide explanations for them.

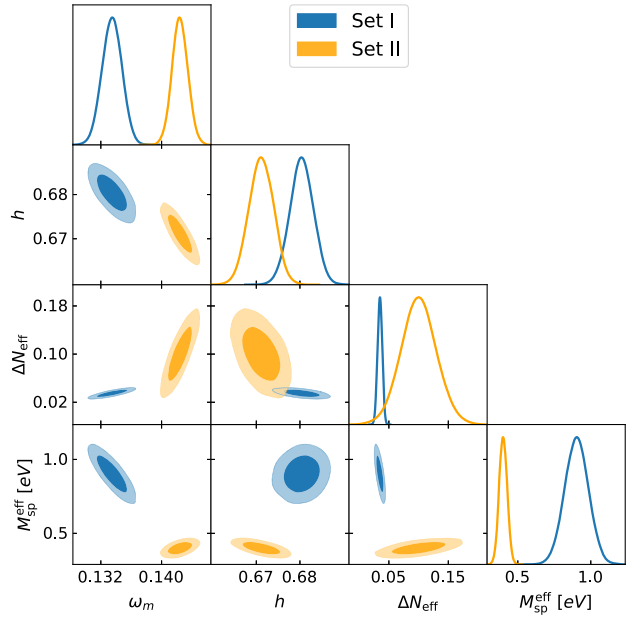

FIG. 5. Comparative Fisher plots for CMB-S4.

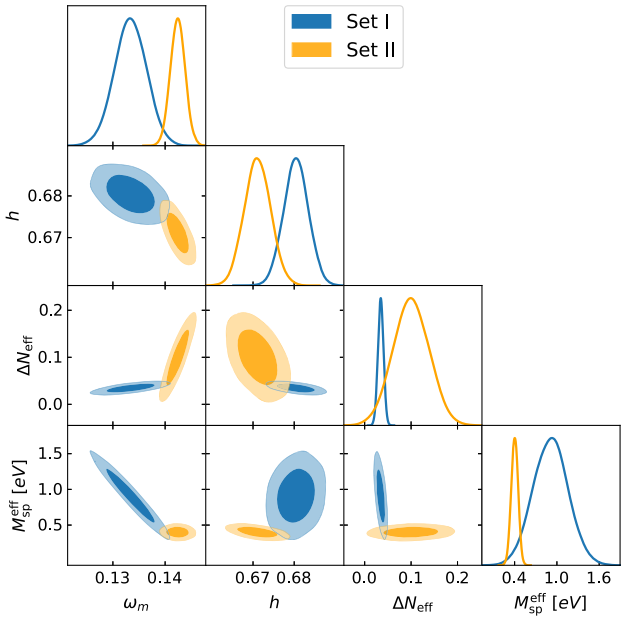

FIG. 6. Comparative Fisher plots for SO-LAT.

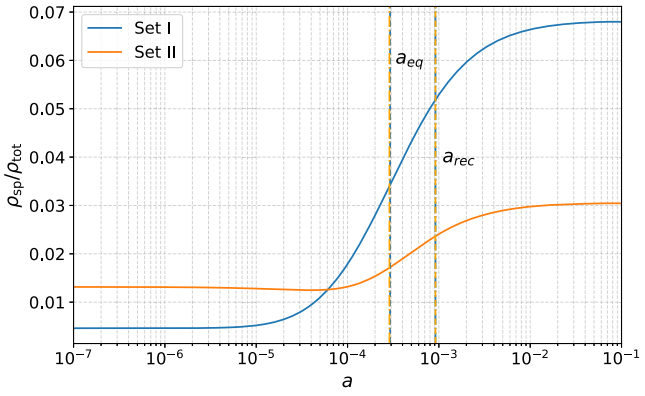

(a)

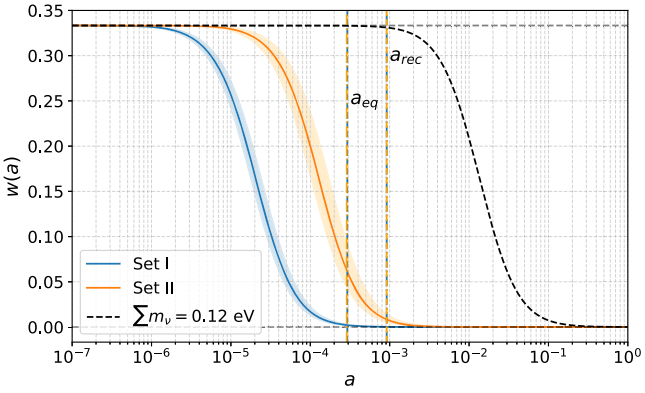

(b)

FIG. 7. Comparison of the evolution of the equation of state parameter and the energy density of the LiMR for the two sets of fiducial values (for the NT model). (a) Evolution of the energy density ρ_{sp} of the particle, as a fraction of the total energy density ρ_{tot} of the Universe, with the scale factor. (b) w vs a plot for the LiMRs corresponding to the two sets of fiducial values. For reference, we have also shown the behavior of massive standard (degenerate) neutrinos with $\sum m_\nu = 0.12\,eV$. The shaded regions correspond to the 1σ uncertainties on w from CMB-S4.

First, let us look at bullet point (i). We will argue that the large difference in the forecasts on $\Delta N_{\rm eff}$ when considering the two sets of fiducial parameter values within the same model arises from the LiMR's contribution to the energy budget just prior to recombination, in particular their relative contributions to the "matter" (with energy density scaling as a^{-3}) and "radiation" (energy density scaling as a^{-4}) components. The heavier particle (set I), owing to its lower number density, has a relatively lesser contribution to the relativistic energy density, compared to the lighter particle (set II), but it contributes significantly more to the matter density, as demonstrated in Fig. 7(a). Evolution of the effective equation of state parameter of the LiMRs are plotted in Fig. 7(b). The heavier particle becomes nonrelativistic just before matter-radiation equality. By recombination, it therefore contributes solely to the total matter density. Contrast this with the lighter particle of set II (contributing more to $N_{\rm eff}$), which is caught in transition at matter-radiation equality and becomes completely nonrelativistic only after recombination. As such, the CMB becomes sensitive to the heavier relic almost exclusively through its effect on the weak lensing signal. When the lensing signal was excluded from the Fisher computations, we obtained $\sigma(\Delta N_{\rm eff}) \sim 0.01(0.04)$ for the heavier (lighter) particle. Even in the absence of lensing, the smaller uncertainty for set I is due to the fact that the particle contributes solely as extra matter by recombination. Any shift in the total matter density at that epoch alters the acoustic peak structure in a way that $\Delta N_{\rm eff}$ (being zero at recombination) cannot mimic. Since $\Delta N_{\rm eff}$ has no freedom to absorb these matterlike changes, the primary spectra pin down its fiducial value to a higher precision. The effect of lensing information is more pronounced in the case of set I (as mentioned above) which leads to a greater improvement in the uncertainty on $\Delta N_{\rm eff}$ (by a factor of $\sim$3) as compared to set II (where there is a $\sim$30% improvement). The heavier LiMR is more degenerate with ω_m at recombination compared to the lighter one—for a given total matter content (baryons + CDM + LiMR), replacing a fraction of ω_m with $\omega_{\rm sp}$ has negligible impact for the heavier particle—this explains the slightly degraded relative uncertainty on $M_{\rm sp}^{\rm eff}$ for set I as compared to set II.

Now we move on to bullet point (ii)—the correlation between the phenomenological parameters. We have summarized the physical origins of the correlations of $\Delta N_{\rm eff}$ with $M_{\rm sp}^{\rm eff}$, as well as with ω_m and h in a schematic flowchart (Fig. 8). The detailed explanations have been relegated to Appendix C, where we also quantitatively validate our qualitative arguments.

V. HIGHER MOMENTS

So far we discussed the impact of LiMRs in terms of two phenomenological parameters $M_{\rm sp}^{\rm eff}$ and $\Delta N_{\rm eff}$ which are proportional to the zeroth and first moments of the phase space distribution function, respectively. We obtained similar results for both the inflaton-decay model and the Dodelson-Widrow model once $M_{\rm sp}^{\rm eff}$ and $\Delta N_{\rm eff}$ are matched, in spite of the noticeably different forms of the distribution functions (see Fig. 1). Reference [47] claimed that different models with the same $M_{\rm sp}^{\rm eff}$ and $\Delta N_{\rm eff}$ would be difficult to distinguish, especially using observables at the linear perturbation theory level. To check how well this claim holds up at the noise levels expected at the CMB-S4 experiment, we consider two distribution functions with matched zeroth and first moments—the Dodelson-Widrow distribution $\hat{f}_{\rm DW}(q)$ and another distribution $\hat{f}(q)$, which starts differing from the Dodelson-Widrow distribution at the level of the second moment. In order to include the effect of the second moment we

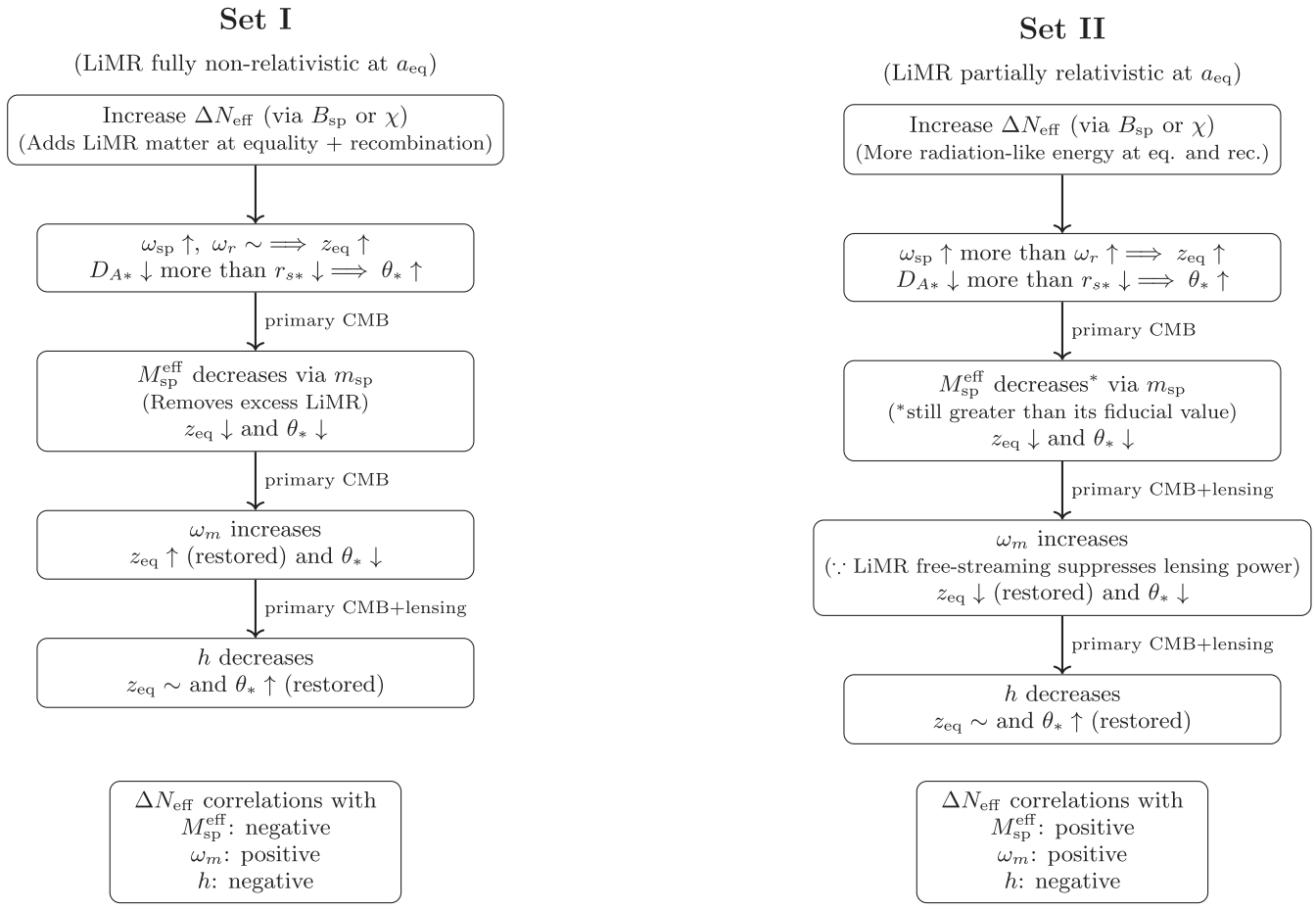

FIG. 8. Schematic flowcharts summarizing the physical origin of parameter correlations for Set I (left) and Set II (right) based (primarily) on $(z_{\rm eq}, \theta_*)$. Labels on the arrows indicate the CMB primary and/or lensing contributions that govern the corresponding step. See Appendix C for details.

consider an Edgeworth-like expansion about the Dodelson-Widrow distribution, which constitutes a continuous deformation of the Dodelson-Widrow distribution,

$$\hat{f}(q) = \hat{f}_{\rm DW}(q)[\alpha_0 P_0(q) + \alpha_1 P_1(q) + \alpha_2 P_2(q)], \quad (31)$$

where $\hat{f}_{\rm DW}(q) = \chi[\exp(q)+1]^{-1}$. The functions $P_m(q)$ are mth order polynomials in q, orthonormal with respect to the measure $q^2/(e^q+1)$ [39],

$$\int_0^\infty dq \frac{q^2}{e^q+1} P_m(q) P_n(q) = \delta_{mn}. \quad (32)$$

The modified distribution function in (31) can be rewritten as

$$\hat{f}(q) = \frac{\chi}{e^q+1}[\alpha + \beta q + \gamma q^2], \quad (33)$$

where α, β, and γ are dimensionless constants, and its nth moment computed as

$$Q^{(n)} = \int_0^\infty dq q^{2+n} \hat{f}(q). \quad (34)$$

Setting $Q^{(0)} = Q^{(0)}_{\rm DW}$ and $Q^{(1)} = Q^{(1)}_{\rm DW}$, i.e., matching the first two moments, we can solve for α and β in terms of γ to obtain

$$\hat{f}(q) = \frac{\chi}{e^q+1}[1 + 13.0551\gamma - 8.24864\gamma q + \gamma q^2], \quad (35)$$

where γ is now a free parameter that determines how much $\hat{f}(q)$ deviates from $\hat{f}_{\rm DW}(q)$. However, to be a valid distribution function, $\hat{f}(q)$ has to be non-negative everywhere. This requirement limits the value of γ to the range $0 \le \gamma \le 0.25$, where $\gamma = 0$ corresponds to the DW distribution (see Fig. 9). That $\hat{f}(q)$ goes to zero at large q values is ensured by the $1/(e^q+1)$ factor, which goes like e^{-q} for large q.

The projected 1σ uncertainties on the six ΛCDM and the two phenomenological parameters, obtained from our Fisher analysis with the fiducial values set I, for the cases

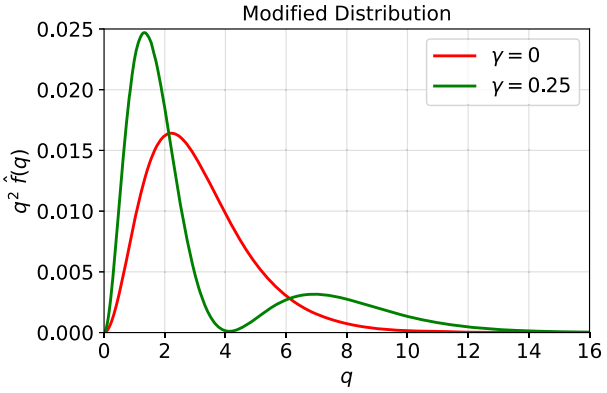

FIG. 9. Plot showing the modified distribution function for $\gamma = 0$ (same as DW) and $\gamma = 0.25$, with the momentum expressed in terms of the neutrino temperature today.

$\gamma = 0$ and $\gamma = 0.25$ are given in Table VI. The corresponding Fisher ellipses and posterior distributions for the phenomenological parameters are shown in Fig. 10.

To determine whether the CMB-S4 experiment will be able to distinguish between these two models, we performed Fisher forecasts by marginalizing over the six ΛCDM parameters, the two phenomenological parameters $\Delta N_{\rm eff}$ and $M_{\rm sp}^{\rm eff}$, along with the γ parameter. In Table VII we show the fiducial values and the projected uncertainties for $\Delta N_{\rm eff}$, $M_{\rm sp}^{\rm eff}$, and γ. Note that increasing the number of parameters being varied worsens the projected uncertainty on each parameter (compare with Table VI). We find that for $\gamma = 0$, the modified distribution with $\gamma = 0.25$ is $\sim 1.4\sigma$ away, and for $\gamma = 0.25$, the DW distribution ($\gamma = 0$) is $\sim 1.5\sigma$ away, when we consider the posterior probability distribution of the γ parameter. This indicates that it is unlikely that CMB-S4 would be able to distinguish between the two distributions at a statistical significance. We believe this generalizes to any two LiMR models having the same values of $\Delta N_{\rm eff}$ and $M_{\rm sp}^{\rm eff}$ irrespective of how much the higher moments differ. However, for the CV limited experiment, the two models were found to be distinguishable (see Table VII): when assuming the $\gamma = 0$ case to be the true model, we found the model corresponding to the $\gamma = 0.25$ case to lie outside the $\sim 7.4\sigma$ CL, whereas when considering the latter model to be the true one, the former was found to lie outside the $\sim 3.9\sigma$ CL So a future experiment with lower noise levels (i.e., better sensitivity) than the CMB-S4 experiment, for instance the CMB-HD experiment [77], can potentially differentiate between two models with the same first two moments. Note that the uncertainties on γ have been obtained using

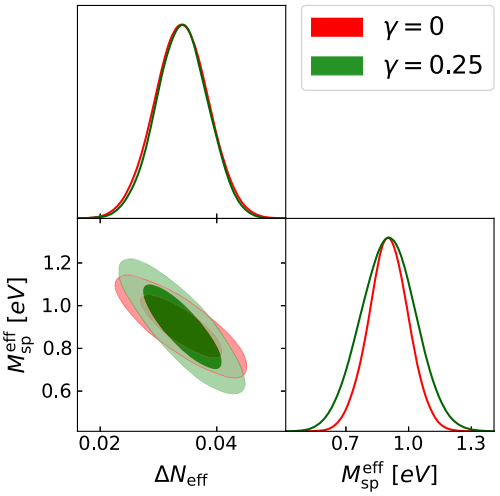

(a)

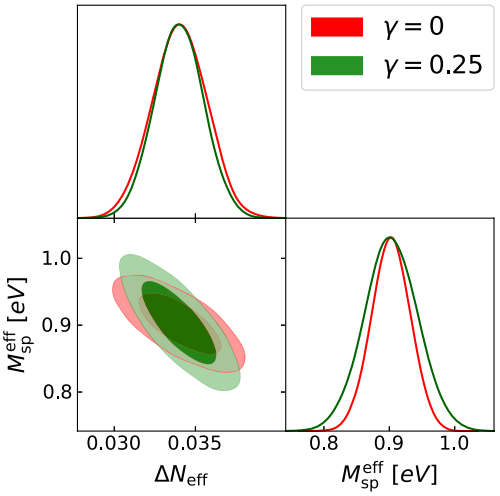

(b)

FIG. 10. Fisher plots of the two phenomenological parameters for the modified distribution. (a) Planck + CMB-S4 forecast. (b) CV-limited experiment forecast.

TABLE VI. Projected uncertainties on the parameters for the modified DW distribution with fiducial values set I.

Experiment	Parameter →	$10^5\omega_b$	$10^3\omega_{\rm cdm}$	H_0	$\ln(10^{10}A_s)$	n_s	$\tau_{\rm reio}$	$\Delta N_{\rm eff}$	$M_{\rm sp}^{\rm eff}$ [eV]
Planck + CMB-S4	1σ error ($\gamma = 0$)	2.74	1.14	0.25	0.0099	0.0019	0.0056	0.0033	0.073
	1σ error ($\gamma = 0.25$)	2.76	1.41	0.23	0.0099	0.0018	0.0056	0.0036	0.110
CV limited	1σ error ($\gamma = 0$)	0.802	0.291	0.093	0.0026	0.00083	0.0014	0.0013	0.0121
	1σ error ($\gamma = 0.25$)	0.806	0.292	0.085	0.0026	0.00083	0.0014	0.0011	0.0133

TABLE VII. Projected uncertainties on the parameters $\{\Delta N_{\rm eff}, M_{\rm sp}^{\rm eff}, \gamma\}$ for the modified DW distribution. Note that the uncertainties on γ are one-sided.

Experiment	$\Delta N_{\rm eff}$	$M_{\rm sp}^{\rm eff}$ [eV]	γ
CMB-S4	0.034 ± 0.0047	0.903 ± 0.097	$0.00^{+0.175}$
	0.034 ± 0.0044	0.903 ± 0.129	$0.25_{-0.168}$
CV-limited	0.034 ± 0.0014	0.903 ± 0.022	$0.00^{+0.034}$
	0.034 ± 0.0013	0.903 ± 0.033	$0.25_{-0.063}$

Eq. (15), and we have not implemented the hard prior on γ, i.e., $0 \leq \gamma \leq 0.25$.

In order to incorporate the valid range of γ in our Fisher analysis, we computed the covariance matrix by numerically sampling a multivariate Gaussian from the inverse of the Fisher matrix and rejecting those realizations for which γ lies outside the allowed range. We obtained the following median values and asymmetric uncertainties (due to the non-Gaussian nature of the posterior distribution induced by the hard prior; see footnote 2):

$$\gamma = 0.098^{+0.088}_{-0.068} \quad \text{and} \quad \gamma = 0.154^{+0.066}_{-0.088}, \tag{36}$$

corresponding to the fiducial values $\gamma = 0$ and $\gamma = 0.25$, respectively. Even with the imposition of the hard priors, which leads to more precise (asymmetric) forecasts, the distribution with $\gamma = 0.25$ is within the 3σ uncertainty threshold of the $\gamma = 0$ distribution and vice versa. This shows that including the hard prior does not change our conclusion above and moving on we shall use the one-sided uncertainties on γ obtained previously. Figure 11 shows the truncated posterior distributions, marginalized only over the six ΛCDM parameters. We quantify the distinguishability between the two cases by computing the overlap fraction between the (un-normalized) posterior probability distributions. The analysis reveals a ∼45% probability

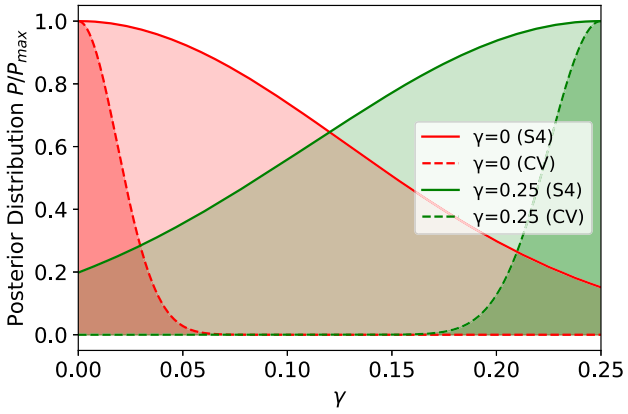

FIG. 11. Comparison of the (normalized) posterior distributions of the parameter γ for the modified DW distribution.

TABLE VIII. Fiducial values and predicted constraints for the quantity f_P.

Experiment	$f_P[\gamma = 0]$	$f_P[\gamma = 0.25]$
CMB-S4	$0.180^{+0.260}$	$0.265_{-0.301}$
CV-limited	$0.180^{+0.050}$	$0.265_{-0.094}$

mass overlap reaffirming that CMB-S4 data would not be able to conclusively distinguish between these models. The expected sensitivity of SO-LAT being less than that of the CMB-S4 survey, this then implies that the Simons Observatory would also not be able to distinguish between these models.

The physical quantity related to the second moment of the LiMR distribution function is the "pressure" of the LiMRs. We define the quantity f_P, the *fractional pressure* of the LiMRs, as (g_s'' is a degeneracy factor)

$$f_P \equiv \frac{P_{\rm sp}}{P_\nu} = \frac{g_s''}{15/16} \underbrace{\left[\int dp p^4 \hat{f}(p)\right]}_{Q^{(2)}} \Big/ \left[\frac{45\zeta(5)}{2}(T_\nu^{\rm id})^5\right]. \tag{37}$$

While the fiducial values of all the ΛCDM parameters as well as that of $\Delta N_{\rm eff}$ and $M_{\rm sp}^{\rm eff}$ are the same, the fiducial values of f_P differ between the cases $\gamma = 0$ and $\gamma = 0.25$. This is a consequence of differing second moments as mentioned above. The fiducial values of f_P and the projected uncertainties (one-sided) are given in the following table: where we have translated the uncertainties on γ to those on the second moment by using $Q^{(2)} = Q^{(2)}_{\rm DW}(= 0.79325) + 1.4865\gamma$. The fact that $f_P + \sigma(f_P)$ for $\gamma = 0$ exceeds 0.265 or $f_P + \sigma(f_P)$ becomes negative for $\gamma = 0.25$ (in the first row in Table VIII), both of which are unphysical, is partly due to the non-Gaussian nature of the posteriors and mostly because of the inadequate sensitivity of the CMB-S4 experiment. In Fig. 12, we plot the equation of state parameter w as a function of the scale factor for the modified distribution, for $\chi = 0.034$ and $m_{\rm sp} = 26.43$ eV, with $\gamma = 0$ and $\gamma = 0.25$. The difference between the two curves arises from the difference in the pressures, or equivalently f_P, and not from $\rho_{\rm sp}$, which is the same for both cases. The inset plot zooms in on a region of the curves and shows the 1σ uncertainties on w, derived from the uncertainties on γ. The overlap between the pink and green shaded regions again indicates that CMB-S4 data would not be able to rule out one model in favor of the other.

If we include a δy^3 term in the expansion (33) and match the first three moments, we find that the new parameter δ can lie in the range [0, 0.015], where the upper bound on the free parameter δ is an order of magnitude lesser than

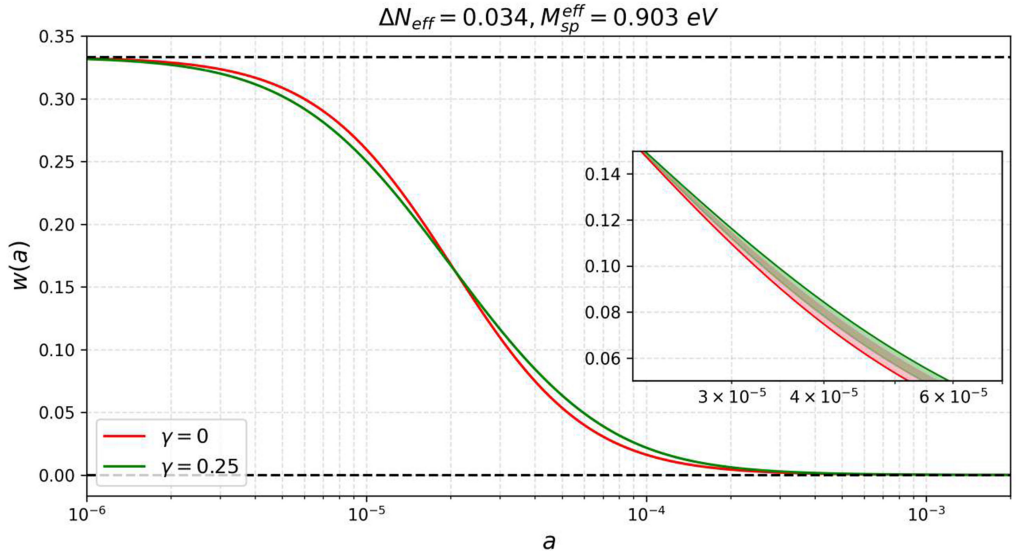

FIG. 12. w vs a plot for the modified distribution (35) with $\gamma = 0$(DW) and $\gamma = 0.25$. Shaded regions in the inset corresponds to the one-sided uncertainties on w derived from the uncertainties on γ.

that on the free parameter γ of the previous case. This suggests that matching the first three moments essentially fixes the form of the modified distribution function with little room for deviation from the DW case. Similar to Fig. 12, in Fig. 13, we plot the evolution of the equation of state parameter w as a function of the scale factor a for the new modified distribution with $\delta = 0$ and $\delta = 0.015$. We find that the curves corresponding to $\delta = 0$ and $\delta = 0.015$ overlap. Thus we conclude that no future CMB experiment would be able to distinguish between two LiMR models which agree on the first three moments of the corresponding LiMR distribution functions. This is likely to generalize to the case of matching even higher moments. Note that this conclusion may not extend to nonlinear scales, a matter that is currently under investigation.

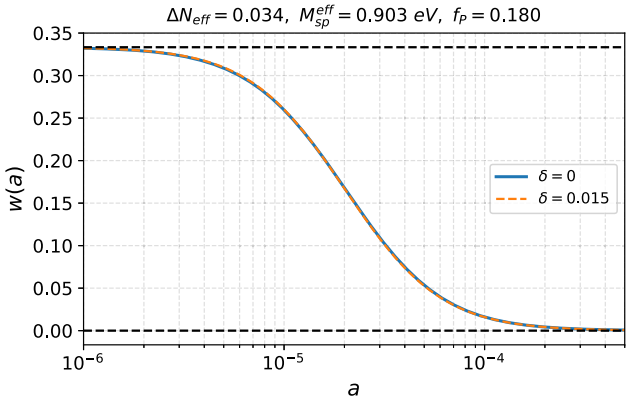

FIG. 13. Evolution of w with a for the DW and the modified distribution when the first three moments are matched and the fourth moment is made to differ by the maximum possible extent. The exact overlap between the curves indicates the indistinguishability of the two models.

VI. CONCLUSION

The presence of LiMRs affects the evolution of the Universe. When relativistic, they behave as dark radiation and contribute to the relativistic energy density of the Universe, whereas when nonrelativistic, they behave as dark matter. The upcoming CMB experiments are expected to measure various cosmological parameters with unprecedented precision. In the context of light relics, $N_{\rm eff}$ is an important parameter. If the measured value of $N_{\rm eff}$ exceeds the SM prediction of 3.044, it would indicate the presence of dark sector light relics (or the need to modify the thermal history of the Universe). SO is expected to achieve a sensitivity of $\sigma(\Delta N_{\rm eff}) = 0.045$ [72] and conservative configurations of the CMB-S4 experiment could reach $\sigma(N_{\rm eff}) \sim 0.02$–$0.03$ [12]. For LiMRs, another important parameter is the relic mass, or rather its contribution to the nonrelativistic energy density of the Universe today, captured by the parameter $M_{\rm sp}^{\rm eff}$. Another important aspect of particles contributing to $N_{\rm eff}$ is their momentum distribution, which is often tied to interesting aspects of the physics of the early Universe and particle physics such as production mechanism and interaction rates. Therefore, extracting the relation between distribution functions and observables is an important question.

In this work, we performed Fisher analyses to check how much future CMB data would be able to constrain these parameters for *nonthermal* LiMR models. We primarily concerned ourselves with a model of inflaton/moduli decay giving rise to LiMRs of mass $m_{\rm sp}$, with a branching ratio $B_{\rm sp}$. The LiMRs so produced follow a nonthermal distribution, unlike thermalized LiMRs, which follow Fermi-Dirac or Bose-Einstein distribution, depending on the statistics [35,78]. We also considered the

Dodelson-Widrow distribution throughout. The main conclusions of our work are as follows:

(i) Our Fisher analysis predicts a tighter constraint on $\Delta N_{\rm eff}(\sim 10^{-3})$ for a LiMR, which becomes nonrelativistic well before recombination, around the epoch of matter-radiation equality. However, the projected uncertainty so obtained might be misleading owing to the fact that the LiMR does not contribute to $\Delta N_{\rm eff}$ at recombination, which is a measure for additional "relativistic" degrees of freedom. The smaller projected uncertainty (further enhanced by lensing) is owing to the fact that changes in $\omega_m (= \omega_b + \omega_{\rm cdm})$ or $\omega_{\rm sp}$ cannot be replicated by changes in $\Delta N_{\rm eff}$, which is zero by recombination. For a LiMR, which transitions in the matter dominated era and becomes completely nonrelativistic just after recombination, we obtained a less precise forecast on $\Delta N_{\rm eff}(\sim 10^{-2})$ in line with the expected uncertainty for light relics [12,72].

(ii) Our analysis is Sec. IV B (see Fig. 4) also revealed interesting correlations between model parameters and observables. In particular, we obtained negative correlation between the phenomenological parameters for set I but positive correlation for set II. These can be relevant in endeavors to connect cosmology with particle physics model building.

(iii) We compared our results for the nonthermal model with those of the Dodelson-Widrow model, and found that CMB-S4 data would yield similar constraints on the parameters for these models once the phenomenological parameters $\Delta N_{\rm eff}$ and $M_{\rm sp}^{\rm eff}$ (related to the first two moments of the distribution function) are matched.

(iv) We also compared the Dodelson-Widrow distribution with a modified distribution (which can be considered as a perturbed Dodelson-Widrow distribution), artificially constructed so as to match the first two moments but differing to the maximum possible extent in the higher moments. We deduced that CMB-S4 data would be unable to tell even these two distributions apart. We believe this generalizes to any two distribution functions with matching first two moments.

LiMRs not only affect the CMB primary and lensing power spectra but also affect the matter power spectrum due to their free streaming/clustering effects. In fact, the effects on the matter power spectrum feed back to the CMB lensing power spectrum. As such, future galaxy surveys such as LSST and Euclid [Vera Rubin Observatory (VRO)] can also probe the impact of LiMRs, and one can perform Fisher analyses for such galaxy surveys. Combining CMB and LSS information is crucial for obtaining optimal constraints on LiMRs, particularly for those relics that are not fully relativistic at recombination, as has been observed in Ref. [35], for example. This we keep for future work. Moreover, going beyond linear theory to the nonlinear matter power spectrum unlocks new information about LiMRs—chiefly through the distinctive, scale-dependent damping they induce, which cannot be mimicked by simply retuning the ΛCDM parameters [79]. This indicates that degeneracies that exist on large (linear) scales can be broken by using signatures on small (nonlinear) scales. In Ref. [79], the authors also found that nonlinear effects can reveal differences between LiMR models that appear identical at the linear level. Remarkably, these distinctions arise from differences in the momentum distribution functions of LiMRs. Since these distributions are intimately connected to the production mechanisms of nonthermal relics, the resulting nonlinear signatures could provide valuable insight into early Universe physics—insight that linear analyses, including the present study, are inherently insensitive to.

ACKNOWLEDGMENTS

The authors thank the anonymous referee whose suggestions helped us improve this paper significantly. R. K. S. thanks the Alexander von Humboldt Foundation for their support. A. B. acknowledges support from the Science and Engineering Research Board (SERB) India via the Startup Research Grant No. SRG/2023/000378.

DATA AVAILABILITY

The data are not publicly available. The data are available from the authors upon reasonable request.

APPENDIX A: INFLATON/MODULI DECAY MODEL

In this appendix, we discuss briefly the production mechanism leading to the form of the nonthermal distribution function (4) for the LiMRs. Further details can be found in Ref. [43]. We start with a matter-dominated Universe at a (dimensionless) "initial time"($\theta \equiv t/\tau = 0$) and evolve the Universe using the following equations up to a time θ^* which is large enough to ensure that almost all the ϕ particles have decayed[10]:

$$\dot{\rho}_m + 3H\rho_m = -\frac{\rho_m}{\tau}, \tag{A1}$$

$$\dot{\rho}_r + 4H\rho_r = +\frac{\rho_m}{\tau}, \tag{A2}$$

and

$$H = \frac{\dot{a}}{a} = \sqrt{\frac{\rho_m + \rho_r}{3M_{\rm Pl}^2}}, \tag{A3}$$

[10]We choose $\theta^* = 15$ in practice.

where $\rho_m = \rho_\phi$ denotes the energy density in matter and $\rho_r = \rho_{\rm sp} + \rho_{\rm SM}$ is the energy density in radiation. As a result of decays, the comoving inflaton/modulus number density falls off as $N(t) = N(0)e^{-t/\tau}$ where

$$N(0) \equiv \frac{\rho_m(0)}{m_\phi} = \frac{4\alpha M_{\rm Pl}^2}{3\tau^2 m_\phi} \quad (\alpha \gg 1). \tag{A4}$$

Combining this with the fact that the energy of a particle produced at $t = t_d$ will evolve according to [with $\hat{E} = E(t_d)$]

$$E(t) = \hat{E}\left(\frac{a(t_d)}{a(t)}\right) = \frac{m_\phi}{2}\left(\frac{a(t_d)}{a(t)}\right), \tag{A5}$$

one can get the physical number density spectrum of the particles,

$$\begin{aligned} dN_t &= \frac{1}{a^3(t)}\frac{2B_{\rm sp}}{\tau}N(0)e^{-t_d/\tau}dt_d \\ &= \frac{2B_{\rm sp}}{\hat{s}^3(\theta)\tau}N(0)e^{-\hat{s}^{-1}(y)}\frac{dE}{E\hat{H}(\hat{s}^{-1}(y))}, \end{aligned} \tag{A6}$$

where we have introduced the variable $y \equiv E\hat{s}(\theta)/\hat{E}$. The number density spectrum is nonvanishing when y varies between 1 (corresponding to decays at the initial time) and $\hat{s}(\theta)$ (corresponding to decays at θ). Using isotropy we can write

$$dN_t = \tilde{n}(E)dE = \frac{\tilde{n}_t(|\boldsymbol{p}|)}{4\pi|\boldsymbol{p}|^2}d^3p \equiv n_t(\boldsymbol{p})d^3p, \tag{A7}$$

where $n_t(\boldsymbol{p}) = n_{t^*}(\frac{a(t)}{a(t_*)}\boldsymbol{p})$ since the sterile LiMRs free stream after production. The bounds on y translate to those on $|\boldsymbol{p}|$; $n_{t_0}(\boldsymbol{p})$ is nonvanishing if

$$\frac{\hat{E}}{a(t_0)} < |\boldsymbol{p}| < \frac{\hat{E}a(t^*)}{a(t_0)}. \tag{A8}$$

One hence arrives at the following late-time momentum distribution function by red-shifting the energy of the particles from their time of production

$$f(\boldsymbol{q}) = \frac{32}{\pi\hat{E}^3}\left(\frac{N(0)B_{\rm sp}}{\hat{s}^3(\theta^*)}\right)\frac{\exp\left(-\hat{s}^{-1}(y)\right)}{|\boldsymbol{q}|^3\hat{H}(\hat{s}^{-1}(y))}, \tag{A9}$$

where $y = (|\boldsymbol{q}|/4)\hat{s}(\theta^*)$ and $|\boldsymbol{q}|$ is constrained so that

$$\frac{4}{\hat{s}(\theta^*)} < |\boldsymbol{q}| < 4. \tag{A10}$$

The argument of the distribution function is $|\boldsymbol{q}| \equiv |\boldsymbol{p}|/T_{\rm ncdm,0}$ where [43]

$$T_{\rm ncdm,0} = 0.418\left(\frac{m_\phi^2\tau}{M_{\rm Pl}}\right)^{1/2}\frac{T_{\rm cmb}}{(1-B_{\rm sp})^{1/4}} \equiv \zeta T_{\rm cmb} \tag{A11}$$

is the temperature of the non-cold-dark-matter species today, expressed in terms of the CMB temperature.

The expressions for the phenomenological parameters are obtained as follows. $\Delta N_{\rm eff}$ is given by

$$\begin{aligned} \Delta N_{\rm eff} &\equiv \left.\frac{\rho_{\rm sp}}{\rho_\nu}\right|_{\nu,\rm dec.} = \left.\frac{\rho_{\rm SM}}{\rho_\nu}\right|_{\nu,\rm dec.} \times \left.\frac{\rho_{\rm sp}}{\rho_{\rm SM}}\right|_{\nu,\rm dec.} \\ &= \left.\frac{g_{*\rm SM}}{g_{*\nu}}\right|_{\nu,\rm dec.} \times \left(\frac{g_*(T(t_\nu))}{g_*(T(t^*))}\right)^{1/3}\frac{B_{\rm sp}}{1-B_{\rm sp}} \\ &= \frac{10.75}{1.75}\left(\frac{g_*(T(t_\nu))}{g_*(T(t^*))}\right)^{1/3}\frac{B_{\rm sp}}{1-B_{\rm sp}}, \end{aligned} \tag{A12}$$

which is typical for models of inflaton/modulus decay to dark radiation particles (see, for example, Refs. [40,80]). Now $\omega_{\rm sp}$ (and hence $M_{\rm sp}^{\rm eff}$) can be obtained by taking the ratio of the number density of LiMRs at t^*, $n_{\rm sp}(t^*) = 2B_{\rm sp}N(0)/a^3(t^*)$, and the entropy density at t^*, $s(t^*) = \frac{4}{3}\rho_{\rm SM}^3(t^*)(\frac{\pi^2}{30}g_*(t^*))^{1/4}$, and using the fact that this ratio is conserved after t^*. The present day LiMR number density $n_{\rm sp,0} = \frac{n_{\rm sp}(t^*)}{s(t^*)}s_0$ can in turn be expressed in terms of $n_{\nu,0}$, which upon substituting in

$$\omega_{\rm sp} = m_{\rm sp}n_{\rm sp,0}\left(\frac{h^2}{\rho_c^0}\right), \tag{A13}$$

and multiplying the resulting expression by 94.05 eV yields Eq. (7).

APPENDIX B: NUMERICAL DERIVATIVES

The numerical differentiation was done using the three-point central difference formula with equal left and right step sizes (for two-sided derivatives)

$$\frac{\partial C_\ell(\theta_0)}{\partial\theta} = \frac{C_\ell(\theta_0+\Delta s) - C_\ell(\theta_0-\Delta s)}{2\Delta s}, \tag{B1}$$

or the two-point forward/backward difference formula (for one-sided derivatives)

$$\begin{aligned} \left.\frac{\partial C_\ell(\theta_0)}{\partial\theta}\right|_+ &= \frac{C_\ell(\theta_0+\Delta s) - C_\ell(\theta_0)}{\Delta s}, \\ \left.\frac{\partial C_\ell(\theta_0)}{\partial\theta}\right|_- &= \frac{C_\ell(\theta_0) - C_\ell(\theta_0-\Delta s)}{\Delta s}. \end{aligned} \tag{B2}$$

Here θ_0 is the fiducial value of the parameter θ under consideration and Δs is the step size. We have not accounted for the dependence of $N_\ell^{\phi\phi}$ on the

TABLE IX. Fiducial values and step sizes (reported as percentage of fiducial value) for the six ΛCDM parameters and the NT model parameters used in the Fisher analysis for the two sets of fiducial values considered in the text.

	Fid. val. Set I		Fid. val. Set II	
Parameter	Fiducial	Step	Fiducial	Step
ω_b	0.02247	1.6%	0.02242	6%
$\omega_{\rm cdm}$	0.111	4%	0.120	4%
h	0.6804	3%	0.6711	3%
$10^9 A_s$	2.099	1%	2.110	1%
n_s	0.9661	1%	0.9652	1%
$\tau_{\rm reio}$	0.0536	4%	0.0560	6.4%
$B_{\rm sp}$	0.0118	1.6%	0.0332	5%
$m_{\rm sp}$ [eV]	38.62	8%	6.2	5%

parameters (through the C_ℓ values) while computing the derivatives—$N_\ell^{\phi\phi}$'s were kept fixed at their fiducial values.

Numerical derivatives play a crucial role in Fisher analysis, and in the computation of numerical derivatives, the choice of step sizes is important. Too large a step size misses fine features and introduces systematic errors, while derivatives are prone to numerical noise and round off errors if the step size is too small. To check for the convergence of the derivatives, we plotted the derivatives with step sizes Δs (given in Table IX for the NT model), $\Delta s/2$ and $2\Delta s$. We first visually inspected the derivatives to check that the curves overlap across multipoles, and then computed two diagnostic quantities,

$$\epsilon_1 = \frac{\sum_\ell |C'_\ell(\Delta s) - C'_\ell(\Delta s/2)|}{\sum_\ell |C'_\ell(\Delta s)|}, \tag{B3}$$

$$\epsilon_2 = \frac{\sum_\ell |C'_\ell(2\Delta s) - C'_\ell(\Delta s)|}{\sum_\ell |C'_\ell(\Delta s)|}, \tag{B4}$$

and checked that $\epsilon_{1,2} \lesssim 10^{-2}$. In Fig. 14, we show the convergence of the derivatives of C_ℓ^{TT}, C_ℓ^{EE}, and $C_\ell^{\phi\phi}$ with respect to the model-specific parameters $B_{\rm sp}$ and $m_{\rm sp}$ for the NT model (set I). Although small oscillatory differences are visible at low multipoles ($\ell \lesssim 100$) for some parameters (like $m_{\rm sp}$) we verified that excluding $\ell < 100$ has a negligible impact on our results pertaining to the phenomenological parameters (and for most cases, we found $\epsilon_{1,2} \sim 10^{-3}$ when we excluded the $\ell < 100$ region). In Fig. 15, we compare the numerical derivatives of C_ℓ^{TT}, C_ℓ^{EE}, and $C_\ell^{\phi\phi}$ with respect to two parameters, $\omega_{\rm cdm}$ and $B_{\rm sp}$, for both sets of fiducial values. We see that the derivatives with respect to $\omega_{\rm cdm}$ are nearly identical for both parameter sets. This observation holds for all six ΛCDM parameters, which indicates that the direct effect of these parameters on the CMB spectra is dominant and largely independent of the specific LiMR properties. In contrast, the derivatives with respect to $B_{\rm sp}$ (and also $m_{\rm sp}$) are significantly different between the two parameter sets, which highlights the sensitivity of the CMB power spectra to the LiMR properties, like its branching ratio and its mass. Computationally, this is the primary source of the difference in the uncertainty values in $\Delta N_{\rm eff}$ and $M_{\rm sp}^{\rm eff}$ between the two sets of

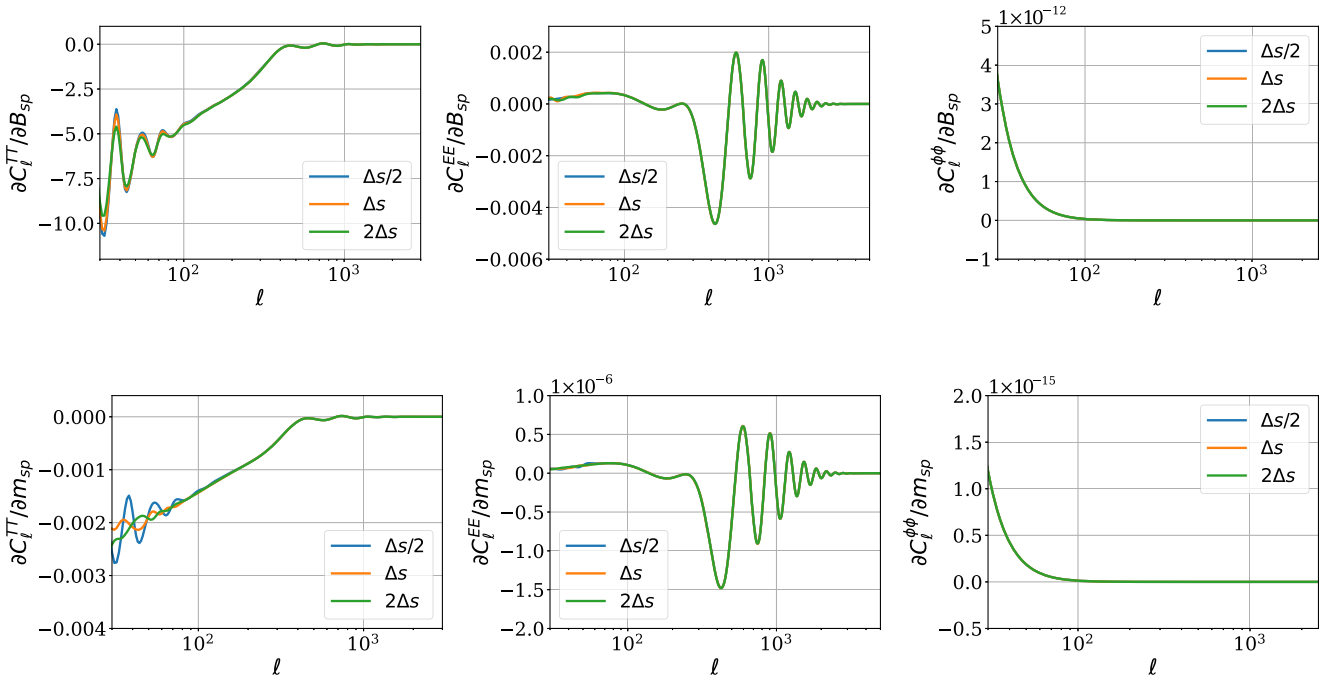

FIG. 14. Convergence plots for the derivatives of the CMB primary and lensing power spectra with respect to $B_{\rm sp}$ (top) and $m_{\rm sp}$ (bottom) for the NT model (set I).

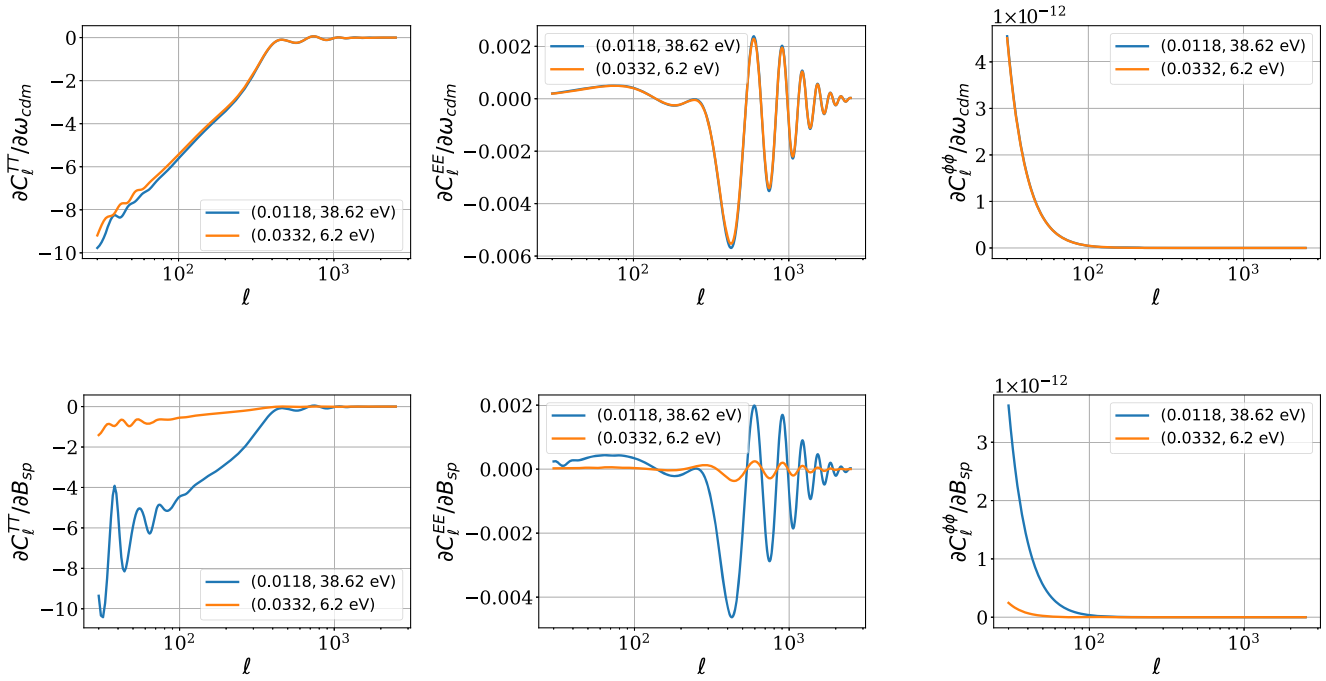

FIG. 15. Comparative plots for the derivatives of the CMB primary and lensing power spectra with respect to $\omega_{\rm cdm}$ (top) and $B_{\rm sp}$ (bottom) for the NT model for the two sets of fiducial values.

fiducial values for the NT model. Similar arguments hold for the DW model.

APPENDIX C: EXPLANATION OF PARAMETER CORRELATIONS

First, let us consider the heavier LiMR of set I. Increasing the LiMR's contribution to $\Delta N_{\rm eff}$ (by increasing $B_{\rm sp}$ or χ) only adds to the matter content (through $M_{\rm sp}^{\rm eff}$) around matter-radiation equality as well as at recombination. This has the following consequences: (a) a greater decrease in the angular diameter distance at recombination D_{A*} as compared to the sound horizon at recombination r_{s*}, thereby increasing $\theta_* = r_{s*}/D_{A*}$, and (b) shifting $z_{\rm eq}$ to an earlier time. Both θ_* and $z_{\rm eq}$ are well constrained by observations [5]. Because late-time LiMR abundance scales linearly with the LiMR mass $m_{\rm sp}$ for a fixed comoving number density ($\propto B_{\rm sp}$ or χ), decreasing $M_{\rm sp}^{\rm eff}$ (via $m_{\rm sp}$) removes the extra LiMR matter introduced, leaving the early relativistic energy density essentially unchanged. The increased radiation content in the early Universe is offset by increasing ω_m, which restores $1+z_{\rm eq} \propto (\omega_m+\omega_{\rm sp})/\omega_r$ to its fiducial value. Although changing only $M_{\rm sp}^{\rm eff}$ or ω_m appropriately could, in principle, keep $z_{\rm eq}$ unchanged, such substitutions are disfavored since LiMR cannot mimic CDM at early times (for example, CDM tends to suppress early ISW effect while LiMR tends to boost it). Even after compensating the $\Delta N_{\rm eff}$-induced changes through $M_{\rm sp}^{\rm eff}$ and ω_m, the residual fractional shifts in D_{A*} and r_{s*} do not cancel. This leads to a decrease in h (which does not affect $z_{\rm eq}$) in order to keep θ_* (almost) unchanged. Note that this is contrary to what happens for standard (massless) neutrinos—h and $N_{\rm eff}$ are positively correlated [5]. Thus we have explained the negative correlations between $(\Delta N_{\rm eff} - M_{\rm sp}^{\rm eff})$ and between $(\Delta N_{\rm eff} - h)$, and the positive correlation between $(\Delta N_{\rm eff} - \omega_m)$.

For the lighter particle of set II, the situation is somewhat different. Now the epoch of matter-radiation equality is set by

$$\rho_r a_{\rm eq}^{-4} + f_{\rm eq}\rho_{\rm sp} a_{\rm eq}^{-4} = \rho_m a_{\rm eq}^{-3} + (1-f_{\rm eq})\rho_{\rm sp} a_{\rm eq}^{-3},$$

where $f_{\rm eq} = 3w_{\rm sp}(a_{\rm eq}) \approx 0.15$. Increasing $\Delta N_{\rm eff}$ again leads to a decrease in $m_{\rm sp}$, but nevertheless leaves $M_{\rm sp}^{\rm eff}$ larger than its fiducial value because $f_{\rm eq}$ is nonzero. Hence the (weakly) positive correlation between $(\Delta N_{\rm eff} - M_{\rm sp}^{\rm eff})$ (degeneracy direction mostly along $\Delta N_{\rm eff}$). Although a further decrease in $m_{\rm sp}$ so as to offset the increase in $M_{\rm sp}^{\rm eff}$ is allowed in principle, such a change is disfavored due to the following reason. Further lowering $m_{\rm sp}$ would extend the LiMR's free-streaming suppression into scales probed by CMB lensing in a way that cannot be fully compensated by

TABLE X. Quantitative validation of the degeneracies between the set of parameters $\{\Delta N_{\rm eff}, M_{\rm sp}^{\rm eff}, \omega_m = \omega_b + \omega_{\rm cdm}\}$ as they relate to $z_{\rm eq}$ (which is unaffected by changes in h). Fiducial values are shown in italics, and changes are shown in bold font.

ω_m	h	$\Delta N_{\rm eff}$	$M_{\rm sp}^{\rm eff}$ [eV]	$z_{\rm eq}$	% change
			Set I		
0.13347	*0.6804*	*0.034*	*0.903*	*3421.85*	…
0.13347	0.6804	**0.037**	0.972	3439.65	+0.25
0.13347	0.6804	**0.037**	**0.881**	3415.82	−0.44
0.13387	0.6804	**0.037**	**0.881**	3425.36	+0.10
0.13387	**0.6797**	**0.037**	**0.881**	3425.36	+0.10
			Set II		
0.14242	*0.6711*	*0.100*	*0.415*	*3478.92*	…
0.14242	0.6711	**0.113**	0.449	3488.44	+0.27
0.14242	0.6711	**0.113**	**0.421**	3474.04	−0.14
0.14268	0.6711	**0.113**	**0.421**	3480.14	+0.03
0.14268	**0.6709**	**0.113**	**0.421**	3480.14	+0.03

changes in ω_m.[11] Similar arguments as used for set I also explain the positive correlation between $(\Delta N_{\rm eff} - \omega_m)$. Without lensing, we found a weak positive correlation between $(\Delta N_{\rm eff} - h)$. Also the change in the sign of correlation between $M_{\rm sp}^{\rm eff}$ and ω_m (flips from slightly negative to positive) is due to the inclusion of the lensing effects, i.e., not influenced by prerecombination era physics. More ω_m enhances lensing strength, compensating for the suppression due to the relic's free streaming. But this again decreases D_{A*} more than r_{s*}; h then decreases to restore θ_*, i.e., lensing indirectly induces the negative correlation between $(\Delta N_{\rm eff} - h)$. Since a CV-limited experiment is expected to reveal the intrinsic physical correlations between different parameters (particularly those whose degeneracies are not dominated by a low-ℓ, CV-dominated regime), we have tried to explain the correlations seen in Fig. 17.[12] In Table X and Fig. 16 we provide the quantitative validation of our qualitative arguments. In generating the table and the plots, we have considered the NT model (for concreteness) and increased $B_{\rm sp}$ by 2σ followed by increasing/decreasing $\{\omega_b, \omega_{\rm cdm}, m_{\rm sp}, h\}$ by $\leq 2\sigma$.

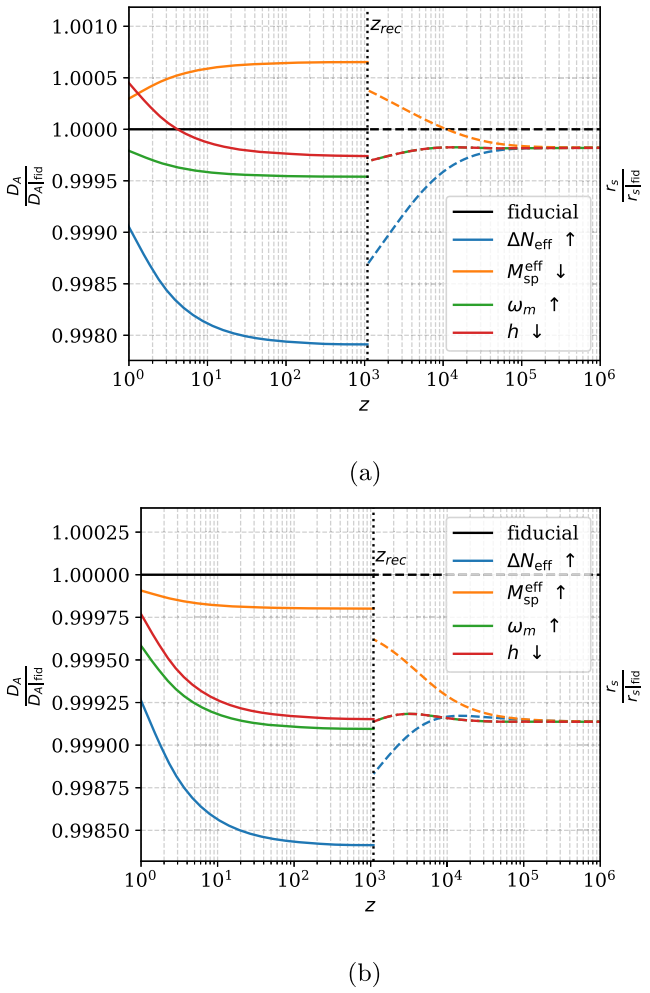

FIG. 16. Quantitative validation of the degeneracies between the set of parameters $\{\Delta N_{\rm eff}, M_{\rm sp}^{\rm eff}, h, \omega_m\}$ as they relate to θ_*; h affects θ_* only through its contribution to D_{A*}. (a) Effect of increasing/decreasing the parameter values (with respect to the fiducial values) on $\theta_* = r_{s*}/D_{A*}$ for set I. (b) Same as (a) for set II.

[11]For the same argument to hold for the LiMR of set I, its mass would need to decrease approximately by an order of magnitude.

[12]In real experiments, low signal-to-noise ratio at higher multipoles can reweight contributions and occasionally flip the apparent sign of a correlation.

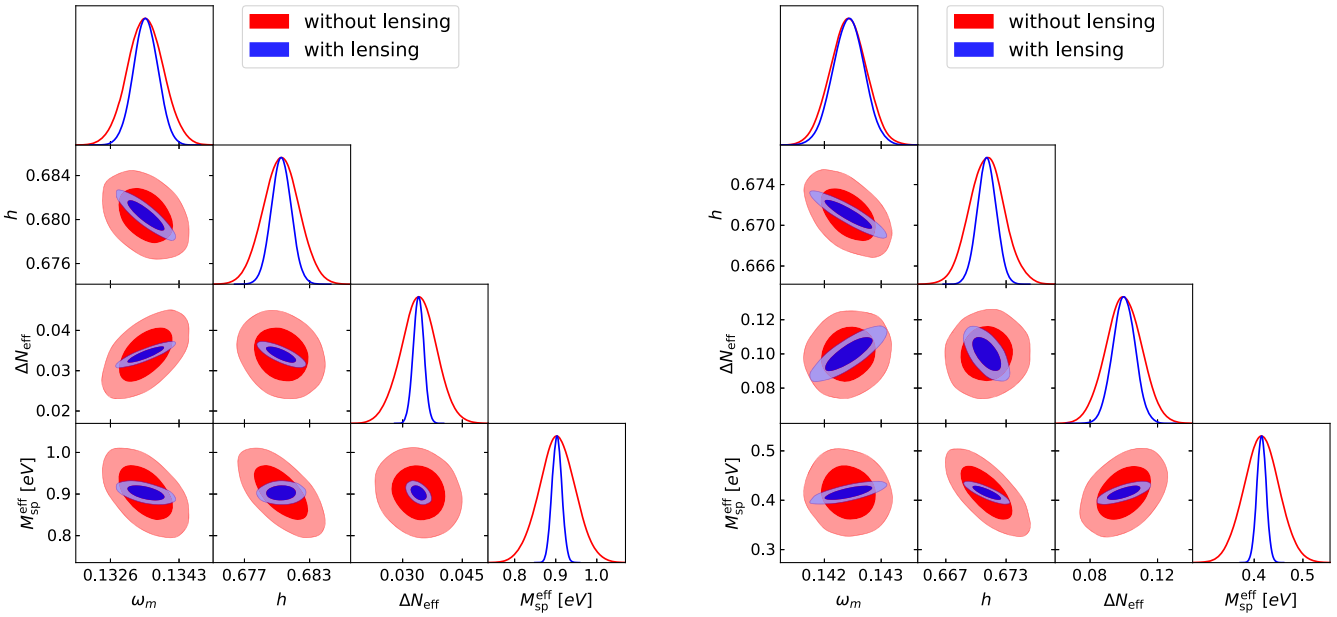

(a) (b)

FIG. 17. Posterior distributions and Fisher ellipses for the parameters $\{\omega_m = \omega_b + \omega_{\rm cdm}, h, \Delta N_{\rm eff}, M_{\rm sp}^{\rm eff}\}$ from the CV-limited experiment. (a) Fisher plots for the NT model, with and without lensing, for fiducial values set I. (b) Same as (a) with fiducial values set II.

[1] Z. Hou, R. Keisler, L. Knox, M. Millea, and C. Reichardt, Phys. Rev. D **87**, 083008 (2013).
[2] B. Follin, L. Knox, M. Millea, and Z. Pan, Phys. Rev. Lett. **115**, 091301 (2015).
[3] D. Baumann, D. Green, J. Meyers, and B. Wallisch, J. Cosmol. Astropart. Phys. 01 (2016) 007.
[4] J. Lesgourgues and S. Pastor, Adv. High Energy Phys. **2012**, 1 (2012).
[5] N. Aghanim *et al.* (Planck Collaboration), Astron. Astrophys. **641**, A6 (2020); **652**, C4(E) (2021).
[6] E. Calabrese *et al.*, J. Cosmol. Astropart. Phys. 11 (2025) 063.
[7] K. Akita and M. Yamaguchi, J. Cosmol. Astropart. Phys. 08 (2020) 012.
[8] J. Froustey, C. Pitrou, and M. C. Volpe, J. Cosmol. Astropart. Phys. 12 (2020) 015.
[9] J. J. Bennett, G. Buldgen, P. F. de Salas, M. Drewes, S. Gariazzo, S. Pastor, and Y. Y. Wong, J. Cosmol. Astropart. Phys. 04 (2021) 073.
[10] A. G. Adame, J. Aguilar, S. Ahlen, S. Alam, D. M. Alexander, M. Alvarez, O. Alves, A. Anand, U. Andrade, E. Armengaud *et al.*, J. Cosmol. Astropart. Phys. 02 (2025) 021.
[11] W. Elbers *et al.*, Phys. Rev. D **112**, 083513 (2025).
[12] Kevork N. Abazajian *et al.* (CMB-S4 Collaboration), arXiv:1610.02743.
[13] K. Abazajian, G. M. Fuller, and M. Patel, Phys. Rev. D **64**, 023501 (2001).
[14] A. Boyarsky, O. Ruchayskiy, and M. Shaposhnikov, Annu. Rev. Nucl. Part. Sci. **59**, 191 (2009).
[15] K. N. Abazajian *et al.*, arXiv:1204.5379.
[16] D. Grin, T. L. Smith, and M. Kamionkowski, Phys. Rev. D **77**, 085020 (2008).
[17] C. Brust, D. E. Kaplan, and M. T. Walters, J. High Energy Phys. 12 (2013) 058.
[18] A. Salvio, A. Strumia, and W. Xue, J. Cosmol. Astropart. Phys. 01 (2014) 011.
[19] M. Kawasaki, M. Yamada, and T. T. Yanagida, Phys. Rev. D **91**, 125018 (2015).
[20] D. Baumann, D. Green, and B. Wallisch, Phys. Rev. Lett. **117**, 171301 (2016).
[21] R. Hložek, D. J. Marsh, D. Grin, R. Allison, J. Dunkley, and E. Calabrese, Phys. Rev. D **95**, 123511 (2017).
[22] L. Visinelli, arXiv:2509.17059.
[23] C. Giunti and M. Laveder, Phys. Rev. D **84**, 073008 (2011).
[24] J. M. Conrad, C. M. Ignarra, G. Karagiorgi, M. H. Shaevitz, and J. Spitz, Adv. High Energy Phys. **2013**, 163897 (2013).
[25] S. Gariazzo, C. Giunti, M. Laveder, and Y. F. Li, J. High Energy Phys. 06 (2017) 135.
[26] A. Aguilar *et al.*, Phys. Rev. D **64**, 112007 (2001).
[27] A. A. Aguilar-Arevalo, B. Brown, L. Bugel, G. Cheng, J. Conrad, R. Cooper, R. Dharmapalan, A. Diaz, Z. D. *et al.*

(MiniBooNE Collaboration), Phys. Rev. Lett. **121**, 221801 (2018).
[28] N. Arkani-Hamed, T. Cohen, R. T. D'Agnolo, A. Hook, H. D. Kim, and D. Pinner, Phys. Rev. Lett. **117**, 251801 (2016).
[29] A. Banerjee, B. Jain, N. Dalal, and J. Shelton, J. Cosmol. Astropart. Phys. 01 (2018) 022.
[30] B. Wallisch, Cosmological Probes of Light Relics, Ph.D. thesis, University of Cambridge, 2018.
[31] S. Bashinsky and U. Seljak, Phys. Rev. D **69**, 083002 (2004).
[32] D. Green *et al.*, Bull. Am. Astron. Soc. **51**, 159 (2019).
[33] Z. Pan and L. Knox, Mon. Not. R. Astron. Soc. **454**, 3200 (2015).
[34] J. Lesgourgues, G. Mangano, G. Miele, and S. Pastor, *Neutrino Cosmology* (Cambridge University Press, Cambridge, England, 2013), 10.1017/CBO9781139012874.
[35] W. L. Xu, J. B. Muñoz, and C. Dvorkin, Phys. Rev. D **105**, 095029 (2022).
[36] N. DePorzio, W. L. Xu, J. B. Muñoz, and C. Dvorkin, Phys. Rev. D **103**, 023504 (2021).
[37] S. Dodelson and L. M. Widrow, Phys. Rev. Lett. **72**, 17 (1994).
[38] X. Shi and G. M. Fuller, Phys. Rev. Lett. **82**, 2832 (1999).
[39] A. Cuoco, J. Lesgourgues, G. Mangano, and S. Pastor, Phys. Rev. D **71**, 123501 (2005).
[40] J. P. Conlon and M. C. D. Marsh, J. High Energy Phys. 10 (2013) 214.
[41] J. Hasenkamp and J. Kersten, J. Cosmol. Astropart. Phys. 08 (2013) 024.
[42] B. S. Acharya, M. Dhuria, D. Ghosh, A. Maharana, and F. Muia, J. Cosmol. Astropart. Phys. 11 (2019) 035.
[43] S. Bhattacharya, S. Das, K. Dutta, M. R. Gangopadhyay, R. Mahanta, and A. Maharana, Phys. Rev. D **103**, 063503 (2021).
[44] S. Baumholzer and P. Schwaller, J. Cosmol. Astropart. Phys. 06 (2022) 013.
[45] V. Mukhanov, *Physical Foundations of Cosmology* (Cambridge University Press, Cambridge, England, 2005), 10.1017/CBO9780511790553.
[46] M. Cicoli, K. Dutta, A. Maharana, and F. Quevedo, J. Cosmol. Astropart. Phys. 08 (2016) 006.
[47] M. A. Acero and J. Lesgourgues, Phys. Rev. D **79**, 045026 (2009).
[48] M. Drees and F. Hajkarim, J. Cosmol. Astropart. Phys. 02 (2018) 057.
[49] R. Allahverdi and J. K. Osiński, Phys. Rev. D **99**, 083517 (2019).
[50] C. Miller, A. L. Erickcek, and R. Murgia, Phys. Rev. D **100**, 123520 (2019).
[51] D. J. H. Chung, E. W. Kolb, and A. Riotto, Phys. Rev. D **60**, 063504 (1999).
[52] G. Gelmini and P. Gondolo, arXiv:1009.3690.
[53] G. B. Gelmini and P. Gondolo, J. Cosmol. Astropart. Phys. 10 (2008) 002.
[54] H. Ganjoo and M. Sten Delos, J. Cosmol. Astropart. Phys. 04 (2024) 015.
[55] H. Bae, A. L. Erickcek, M. S. Delos, and J. B. Muñoz, Phys. Rev. D **112**, 083013 (2025).
[56] R. Allahverdi and J. K. Osiński, Phys. Rev. D **105**, 023502 (2022).
[57] M. Dutra and Y. Wu, Phys. Dark Universe **40**, 101198 (2023).
[58] J. Silva-Malpartida, N. Bernal, J. Jones-Pérez, and R. A. Lineros, J. Cosmol. Astropart. Phys. 03 (2025) 003.
[59] P. Conzinu and G. Marozzi, Phys. Rev. D **108**, 043533 (2023).
[60] A. Banerjee and D. Chowdhury, SciPost Phys. **13**, 022 (2022).
[61] A. Ghoshal, L. Heurtier, and A. Paul, J. High Energy Phys. 12 (2022) 105.
[62] S.-Q. Ling and Z.-H. Yu, Chin. Phys. C **49**, 105105 (2025).
[63] G. Arcadi, arXiv:2406.11042.
[64] R. Durrer, *The Cosmic Microwave Background* 2nd ed. (Cambridge University Press, Cambridge, England, 2020), 10.1017/9781316471524.
[65] M. Tegmark, A. N. Taylor, and A. F. Heavens, Astrophys. J. **480**, 22 (1997).
[66] D. Coe, arXiv:0906.4123.
[67] W. L. K. Wu, J. Errard, C. Dvorkin, C. L. Kuo, A. T. Lee, P. McDonald, A. Slosar, and O. Zahn, Astrophys. J. **788**, 138 (2014).
[68] A. Manzotti, S. Dodelson, and Y. Park, Phys. Rev. D **93**, 063009 (2016).
[69] D. Blas, J. Lesgourgues, and T. Tram, J. Cosmol. Astropart. Phys. 07 (2011) 034.
[70] J. Lesgourgues and T. Tram, J. Cosmol. Astropart. Phys. 09 (2011) 032.
[71] Z. Li, V. Gluscevic, K. K. Boddy, and M. S. Madhavacheril, Phys. Rev. D **98**, 123524 (2018).
[72] M. Abitbol *et al.* (Simons Observatory Collaboration), J. Cosmol. Astropart. Phys. 08 (2025) 034.
[73] M. S. Madhavacheril and J. C. Hill, Phys. Rev. D **98**, 023534 (2018).
[74] A. P. *et al.*, J. Cosmol. Astropart. Phys. 02 (2019) 056.
[75] A. Manzotti, S. Dodelson, and Y. Park, Phys. Rev. D **93**, 063009 (2016).
[76] S. Das, A. Maharana, V. Poulin, and R. K. Sharma, Phys. Rev. D **105**, 103503 (2022).
[77] N. Sehgal *et al.*, arXiv:2002.12714.
[78] D. Baumann, D. Green, and B. Wallisch, J. Cosmol. Astropart. Phys. 08 (2018) 029.
[79] A. Banerjee, S. Das, A. Maharana, and R. Kumar Sharma, Mon. Not. R. Astron. Soc. **516**, 2038 (2022).
[80] M. Cicoli, J. P. Conlon, and F. Quevedo, Phys. Rev. D **87**, 043520 (2013).